



Understanding monsoon controls on the energy and mass balance of Himalayan glaciers

Authors: Stefan Fugger^{1,2}, Catriona L. Fyffe^{1,3}, Simone Fatichi⁴, Evan Miles¹, Michael McCarthy^{1,5}, Thomas E. Shaw¹, Baohong Ding⁶, Wei Yang⁶, Patrick Wagnon⁷, Walter Immerzeel⁸, Qiao Liu⁹, and Francesca Pellicciotti^{1,3}

¹Swiss Federal Institute for Forest, Snow and Landscape Research (WSL), Birmensdorf, Switzerland

²Institute of Environmental Engineering, ETH Zurich, 8093 Zurich, Switzerland

³Department of Geography and Environmental Sciences, Northumbria University, Newcastle, UK

⁴Department of Civil and Environmental Engineering, National University of Singapore, Singapore

⁵British Antarctic Survey, Cambridge, UK

⁶Institute of Tibetan Plateau Research, Chinese Academy of Sciences, Beijing, China

⁷Univ. Grenoble Alpes, CNRS, IRD, Grenoble-INP, IGE, 38000 Grenoble, France

⁸Faculty of Geosciences, Department of Physical Geography, Utrecht University, Utrecht, The Netherlands

⁹Institute of Mountain Hazards and Environment, Chinese Academy of Sciences, Chengdu, China

Correspondence: Stefan Fugger (stefan.fugger@wsl.ch)

Abstract. The Indian and East Asian Summer Monsoons shape the melt and accumulation patterns of glaciers in High Mountain Asia in complex ways due to the interaction of persistent cloud cover, large temperature amplitudes, high atmospheric water content and high precipitation rates. While the monsoons dominate the climate of the southern and eastern regions, they progressively lose strength westward towards the Karakoram, where the influence of Westerlies is predominant. Despite the major role of the monsoon in the Himalayas, a holistic understanding of their influence on the region's glaciers is lacking because previous applications of energy- and mass-balance models have been limited to single study sites. In this study, we use a full energy- and mass-balance model and seven on-glacier automatic weather station datasets from different parts of the Himalayas to investigate how monsoon conditions influence the glacier surface energy and mass balance. In particular, we look at how debris-covered and debris-free glaciers respond differently to monsoonal conditions. The radiation budget mostly controls the melt of clean-ice glaciers, but turbulent fluxes also play an important role in modulating the melt energy on debris-covered glaciers. The sensible heat flux reduces during core monsoon, but the latent heat flux removes energy from the surface due to evaporation of liquid water. This interplay of radiative and turbulent fluxes, together with compensations between increasing and decreasing melt rates over the diurnal cycle, causes debris-covered glacier melt rates to stay almost constant over the entire ablation period through the different phases of the monsoon. Ice melt under thin debris, on the other hand, is amplified by both the dark surface albedo and the turbulent fluxes, which act as a source of energy through surface heating and condensation, especially during monsoon. Pre-monsoon snow cover can considerably delay melt onset and have a strong impact on the seasonal mass balance. Intermittent monsoon snow cover further modulates the melt rates at high elevation. Given our results, we expect the mass balance of debris-covered glaciers to react less sensitively to projected future monsoon conditions than clean-ice and



dirty-ice glaciers. This work is fundamental to the understanding of the present and future Himalayan cryosphere and water
20 budget evolution, while informing and motivating further glacier- and catchment-scale research using process-based models.
(Yang et al., 2017)

1 Introduction

High Mountain Asia (HMA) holds the largest ice volume outside the polar regions (Farinotti et al., 2019) and due to the large
elevation range and vast geographic extent, HMA glaciers are highly diverse in character and hydro-climatic situation (Yao
25 et al., 2012). Several large-scale weather patterns interact with the region's topography (Bookhagen and Burbank, 2010), causing
glaciers to contrast in terms of hypsometry (Scherler et al., 2011a) and accumulation and ablation seasonality (MauSSION
et al., 2014). The Indian Summer Monsoon dominates the Central Himalaya and the Southeastern Tibetan Plateau during summer,
and gradually loses strength moving towards the Karakoram, Pamir and Kunlun ranges in the east, where the influence
of Westerlies is particularly strong. A more continental, monsoon-westerlies-influenced regime controls the Central Tibetan
30 Plateau (Yao et al., 2012; Mölg et al., 2014), and the East Asia Monsoon influences the eastern slopes of the Tibetan Plateau
(MauSSION et al., 2014; Yao et al., 2012). These major modes of atmospheric circulation do not only control the surface processes
and runoff regimes of glaciers (e.g. Mölg et al., 2014, 2012; Kaser et al., 2010) but also lead to distinct responses of
glaciers to climate change (Yao et al., 2012; Sakai and Fujita, 2017; Scherler et al., 2011b; Kraaijenbrink et al., 2017). For example,
35 mass losses are high throughout most of HMA, and are particularly pronounced on the South-Eastern Tibetan Plateau,
while glaciers exhibit a near-balance regime in the Karakoram, Pamir and Kun Lun (Farinotti et al., 2020; Gardelle et al., 2012;
Brun et al., 2017; Shean et al., 2020).

Accurate glacier mass balance modelling is essential to assess glacier meltwater contribution to mountain water resources,
and to predict future glacier states and catchment runoff. Physically-based models of glacier energy- and mass balance represent
surface and sub-surface energy fluxes using physical equations to calculate the energy residual, i.e. the energy available for
40 melt, and the glacier runoff. They have provided an understanding about the individual processes controlling the glacier mass
balance and the climatic sensitivity of glaciers in their specific hydro-climatic environment (e.g. Mölg et al., 2012). Summer-
accumulation type glaciers in HMA experience simultaneous accumulation and ablation and their mass balances are known to
be highly sensitive to climatic variability during the monsoon season (Fujita and Ageta, 2000), when warm air temperatures
and high moisture influx coincide. Using energy balance modelling for an inter-annual study for the Central Tibetan Zhadang
45 glacier, Mölg et al. (2012) demonstrated that the timing of monsoon onset and the associated albedo variability can change
melt-rates substantially in subsequent years. At the same time, they observed a de-coupling of the glacier mass balance from
the Indian Summer Monsoon's control during the core monsoon season. Mölg et al. (2014) explain the mass balance variability
of Zhadang Glacier as being controlled by both the Indian Summer Monsoon onset and remotely controlled by mid-latitude
Westerlies. Combining energy balance with weather forecast modelling, Bonekamp et al. (2019) identify the timing and quan-
50 tity of snowfalls as the main source of differences in mass-balance regimes between the Shimshal Valley in the Karakoram and



the Langtang Valley in the Central Himalaya. Similarly, Zhu et al. (2018) attribute mass balance differences of three glaciers on the Tibetan Plateau mainly to different local rain-/snowfall ratios and timing.

The presence of debris cover, a widespread characteristic of HMA glaciers, (e.g. Herreid and Pellicciotti, 2020; Kraaijenbrink et al., 2017; Scherler et al., 2011b), creates additional complexity to understanding and modelling the processes leading to (sub-debris) glacier melt. In recent years, much effort has gone into developing energy balance models for debris-covered glaciers, (e.g. Fujita et al., 2014; Reid and Brock, 2010; Nicholson and Benn, 2006; Lejeune et al., 2013; Rounce et al., 2015; Evatt et al., 2015; Collier et al., 2014; Steiner et al., 2018). Yang et al. (2017) compares the energy balance of a debris-covered and a clean-ice glacier on the Southeastern Tibetan Plateau and finds the main differences, beside the differences in melt rates, is their climatic sensitivity and the important role of turbulent fluxes on debris-covered glaciers. Thick debris is a stronger control on melt rates than elevation (Shah et al., 2019) and also dampens and delays glacier melt in the diurnal cycle (Shrestha et al., 2020), while melt enhancement can occur where there is very thin or patchy debris (Fyffe et al., 2020). Ablation is often expected to be higher on such 'dirty ice glaciers' than at both clean-ice sites and at sites with established debris cover, as shown experimentally (Reznichenko et al., 2010; Östrem, 1959), and by means of modelling (Reid and Brock, 2010), with humidity being a determining factor for this enhancement (Evatt et al., 2015). Moisture in debris is an important factor under monsoonal conditions, controlling the debris' thermal properties and thus ablation (Sakai et al., 2004; Nicholson and Benn, 2006) and has been the focus of devoted modelling studies (Giese et al., 2020; Collier et al., 2014). Moreover, the representation of latent heat due to evaporation (Giese et al., 2020; Steiner et al., 2018) and atmospheric stability correction for turbulent fluxes were shown to be important to improve the simulation of sub-debris melt (Reid and Brock, 2010; Mölg et al., 2012). Model implementation, however, remains complex and difficult to validate and transfer. Nevertheless, Nicholson and Stiperski (2020) showed that the turbulent conditions over debris-covered and clean-ice sites are similar enough to be numerically treated in similar ways, i.e. the Monin-Obukhov similarity theory can be leveraged in the same way for the calculation of the turbulent fluxes, but with different parameters.

Observations of glacier surface meteorology, a prerequisite for accurate energy balance modelling, exist only for a few glaciers in HMA, and even fewer records exist for debris-covered glaciers. Direct observations of glacier mass balance in HMA also remain sparse, and remote sensing observations are hindered by heavy cloud cover during the monsoon season.

Previous studies explicitly dealing with the imprint of the monsoon on the surface thermal properties of glaciers remained limited to individual clean-ice glaciers in the Central Tibetan Plateau (Mölg et al., 2012, 2014). Our main goal is to improve understanding of monsoon controls on glaciers in the Himalayan region by leveraging available automatic weather station (AWS) records in the region. Our specific objectives are: 1) to understand, in detail, the glacier energy and mass balance and related controls at seven Himalayan study sites in a robust and systematic manner; 2) to assess the effects of monsoonal conditions on debris-covered and clean ice glaciers; 3) to investigate whether these effects are generalisable; and 4) to discuss possible implications of our findings under climate change. We address these objectives by applying the glacier energy and mass balance module of a land surface model suited to both debris-covered and clean-ice glaciers. We apply the model at the point scale of individual AWSs, driven by high-quality in situ meteorological observations that guarantee accurate energy balance simulations, not affected by extrapolation of the meteorological forcing. By identifying and discussing the key surface



processes of glaciers and their dynamics under monsoonal conditions, this study promotes their appropriate representation in models of glacier mass balance and the hydrology of glacierised catchments.

2 Study sites and data

90 2.1 Sites and observations

In situ observations from seven on-glacier automatic weather stations in different environments along the climatic gradient of the Himalayas were gathered and are used for forcing and evaluation of the model (Table 2). Our seven study sites are located in the Central and Eastern Himalayas and cover a range of glacier types and local climates (Figure 1, 2 and Table 1). The seven sites include both spring- (24K, Parlung No.4) and summer-accumulation glaciers (all others) as indicated by the proportion
95 of monsoon precipitation to the annual precipitation (Figure 3). Langtang, Lirung and Yala are neighboring glaciers found in the Langtang Valley (Figure 1), which has an extensive history of glaciological and hydrological research. The Langtang Valley is strongly influenced by the Indian Summer Monsoon (~ June to October), during which more than 70% of the annual precipitation arrives (Figure 3 and Table 1), while the period from November to May is a drier season (Collier and Immerzeel, 2015; Immerzeel et al., 2012). The Langtang Valley has been a site of extensive glaciological (e.g. Fujita et al., 1998; Stumm
100 et al., 2020), meteorological (Immerzeel et al., 2014; Heynen et al., 2016; Steiner and Pellicciotti, 2016; Bonekamp et al., 2019; Collier and Immerzeel, 2015) and hydrological (e.g. Ragettli et al., 2015) investigations. On-glacier AWSs were installed during the ablation season on Lirung (2012-2015) and Langtang (2019) glaciers, and year-round on Yala (2012-ongoing) (Table 2). Both Lirung and Langtang are valley glaciers that have heavily debris-covered tongues, but the tongue of Lirung has disconnected from the accumulation zone (Figure 2). Yala is a considerably smaller clean-ice glacier, with most of its ice mass
105 located at comparably high elevation. It is oriented to the southwest and has a gentle slope (Fujita et al., 1998) (Figure 2 and Table 1).

North Changri Nup Glacier (hereafter Changri Nup Glacier) is a debris-covered valley glacier located in the Everest region in Nepal (Figure 1). The southeast-oriented, avalanche-fed glacier discharges into the Koshi River system. The local climate is similar to the one of the Langtang Valley, with 70-80% of precipitation falling during monsoon (Vincent et al., 2016) (Figure
110 2, 3 and Table 1).

24K and Parlung No.4 glaciers are located on the southeastern Tibetan Plateau, feeding water into the upper Parlung Tsangpo, a major tributary to the Yarlung Tsangpo - Brahmaputra River. The summer climate is characterized by monsoonal air masses reaching the Gangrigabu mountain range from the south through the Yarlung Tsangpo Grand Canyon. 24K Glacier is an avalanche fed valley glacier with a debris-covered tongue, located 24 km from the town of Bome (Yang et al., 2017). It is small
115 in size, oriented to the northwest and surrounded by shrubland (Figure 1, 2 and Table 1). Parlung No.4 is a debris-free valley glacier, which is north-east oriented, considerably larger than 24K and located 130km (south-east) from Bome (Yang et al., 2011) (Figure 1 and Table 1). Full automatic weather stations were installed in the ablation zones of both glaciers in 2016 and subsequent years (Table 2).

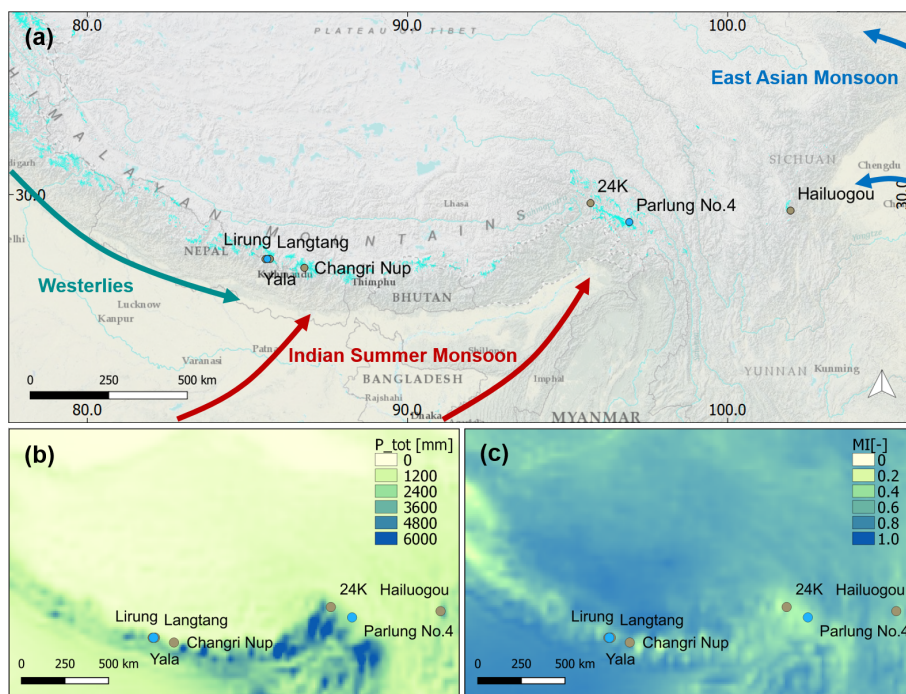


Figure 1. (a) shows the context of study sites with respect to large-scale weather patterns, topography and glacier distribution (turquoise, source: Randolph Glacier Inventory 6.0). Blue dots indicate clean-ice study glaciers and brown dots indicate debris-covered study glaciers. (b) displays the spatial pattern of average annual precipitation from ERA5-Land (1981-2019). (c) shows the monsoonal (June-September) portion of the ERA5-Land total annual precipitation (MI). Background map source: ESRI, U.S. National Park Service.

Hailuogou Glacier, the second-largest of our study sites (Figure 2) is located on the eastern slope of Mt. Gongga in the easternmost portion of the southeastern Tibetan Plateau (Figure 1). It is located at low elevation and covered with thin and patchy debris, leading to high annual ablation rates (Figure 2 and Table 1). The local climate influenced by the East Asia Monsoon with typically only 50 to 60% of the annual precipitation arriving during the monsoon period (Figure 1 and 3). The debris-covered tongue is connected to a steep and extensive accumulation zone via a large icefall, but avalanching is the primary mass supply mechanism through the icefall to the valley tongue (Liao et al., 2020), and a dynamic disconnect is expected to occur in the near future. Weather stations were installed at three nearby off-glacier locations and one on-glacier site during 2008, while precipitation was measured at Alpine Ecosystem Observation and Experiment Station of Mt. Gongga, within 1.5 km from the glacier terminus (Table 2).

2.2 Climatic and meteorological conditions

Here, we use the monthly averaged ERA5-Land reanalysis data (Muñoz Sabater, 2019) to provide an overview of the long term climatic patterns, e.g. the average monsoonal regime from June through September, and evaluate the representativeness



Table 1. Characteristics of the study sites. Planimetric glacier and debris surface areas, mean elevation, slope and aspect were calculated using the updated Randolph Glacier Inventory 6.0 by Herreid and Pellicciotti (2020) and the USGS GTOPO30 digital elevation model. Slope and aspect are mean values for the whole glacier. MI ('Monsoon-Index') is the mean June-September portion of the ERA5-Land total annual precipitation (1981-2019)

	Area [km^2]		Elevation [$m.asl$]			Slope	Aspect	MI
	Glacier	Debris	min	max	mean	[°]	[°]	[-]
Lirung (LIR)	4.0	1.5	3990	6830	5100	27.6	153.1	0.74
Langtang (LAN)	37.0	17.8	4500	6620	5330	16.0	175.2	0.71
Yala (YAL)	1.4	-	5170	5660	5390	23.5	228.2	0.74
Changri Nup (CNU)	2.7	1.4	5270	6810	5610	15.9	183.2	0.76
24K (24K)	2.0	0.9	3910	5070	4350	18.3	273.4	0.46
Parlung No.4 (NO4)	11.0	-	4620	5950	5330	17.1	152.6	0.40
Hailuogou (HAI)	24.5	4.1	2980	7470	5360	27.0	117.5	0.56

Table 2. Summary of available meteorological and ablation observations at each site, as well as each site's model period. Variables indicated with * were transferred from neighboring weather station. Variables with ** were reconstructed based on other variables measured at the same station.

	AWS Location				Variables measured			Model period	Reference
	Lat	Lon	Elevation [m.a.s.l.]	Debris thickness [cm]	AWS	Precipitation	Ablation	begin/ end	
Lirung	28.233	85.562	4076	30	$T, RH, W_s, W_d, SW_{\downarrow}, SW_{\uparrow}, LW_{\uparrow}, LW_{\downarrow}, P_{atm}^*$	Pluvio Kyangang and Yala Basecamp, 3857m.asl and 5090m.asl, hourly, partly lapsed	SR50	2014-05-05/ 2014-10-24	Ragetti et al. (2015)
Langtang	28.279	85.722	4557	50	$T, RH, W_s, W_d, SW_{\downarrow}, SW_{\uparrow}, LW_{\uparrow}^{**}, LW_{\downarrow}, P_{atm}^*$	Pluvio Morimoto base camp 4919m.asl, hourly	SR50	2019-05-11/ 2019-10-30	unpublished
Yala	28.233	85.612	5090	-	$T, RH, W_s, W_d, SW_{\downarrow}, SW_{\uparrow}, LW_{\uparrow}, LW_{\downarrow}, P_{atm}^*$	Pluvio Yala base camp 5090m.asl, hourly	SR50	2019-05-01/ 2019-10-31	ICIMOD (2021)
Changri Nup	27.993	86.780	5471	10	$T, RH, W_s, W_d, SW_{\downarrow}, SW_{\uparrow}, LW_{\uparrow}, LW_{\downarrow}, P_{atm}^*$	Pluvio at Pyramid meteorological station (4993 m a.s.l.), 4.9 km SE of AWS location, hourly	SR50	2016-05-01/ 2016-10-31/	Wagnon (2021)
24K	27.983	86.778	5362	20	$T, RH, W_s, W_d, SW_{\downarrow}, SW_{\uparrow}, LW_{\uparrow}, LW_{\downarrow}, P_{atm}^*$	On-glacier tipping bucket, hourly	stake	2016-06-01/ 2016-09-29	Yang et al. (2017)
Parlung No.4	29.761	95.720	3900	-	$T, RH, W_s, W_d, SW_{\downarrow}, SW_{\uparrow}, LW_{\uparrow}, LW_{\downarrow}, P_{atm}^*$	Pluvio, near terminus 4600m.asl, hourly	stake	2016-05-01/ 2016-10-31	Yang et al. (2017)
Hailuogou	29.558	101.969	3550	1	$T, RH, W_s, W_d, SW_{\downarrow}, SW_{\uparrow}, LW_{\uparrow}, LW_{\downarrow}, P_{atm}^*$	Pluvio at GAEORS station, 3000m.asl, 1.5km from terminus	stake	2008-05-15/ 2008-10-31	Zhang et al. (2011)

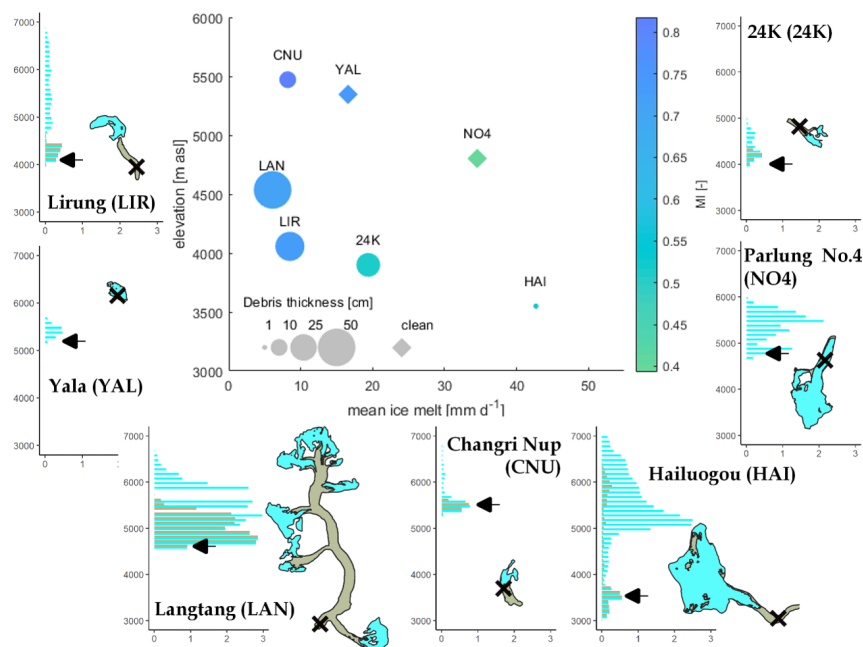


Figure 2. Characteristics of study sites, summarized (center) in terms of elevation, mean measured ice melt rate, measured debris thickness and JJAS contribution to the ERA5-Land total annual (1981-2019) precipitation (monsoon index; MI). For each site, we also show glacier (blue bars) and debris (brown bars) hypsometry, with area on the x-axis [km^2] and altitude on the y-axis [$m.asl$], and glacier and supraglacial debris extents. Black crosses and arrows indicate AWS location on the glacier.

of the AWS records in terms of seasonal variability (Figures A1 to A7), while acknowledging that the absolute values from the reanalysis dataset might be biased.

Incoming shortwave radiation (Figure 3b) shows a clear peak before monsoon onset at all sites. A smaller secondary peak is reached just after the monsoon in October at the Central Himalayan sites, but not at the Eastern Himalayan sites. Interruptions in monsoonal overcast conditions (break periods) seem to be more common at the eastern sites, leading to occasional secondary peaks in incoming shortwave radiation during monsoon.

Average mean monthly 2 m air temperatures have a similar pattern at all study sites (Figure 3a), with a slow increase from January to a peak between July and August, just after peak monsoon, and a steeper decline from post-monsoon into winter. A similar regime is followed by LW_1 , with highest values reached during the core monsoon (Figure 3c).

There is a clear difference in the seasonal evolution of precipitation between the Central (Lirung, Lantang, Yala, Changri Nup) and the Eastern Himalayan sites (24K, Parlung No.4, Hailuogou) (Figure 3e): relatively high mean monthly precipitation during the monsoon period is contrasted by comparably low precipitation outside of this period. The eastern sites have less pronounced monsoonal precipitation peaks, and more gradual changes in precipitation intensities over the annual cycle. The Parlung sites (24K and Parlung No.4) have two precipitation peaks: during spring and monsoon. Hailuogou exhibits the smoothest evolution

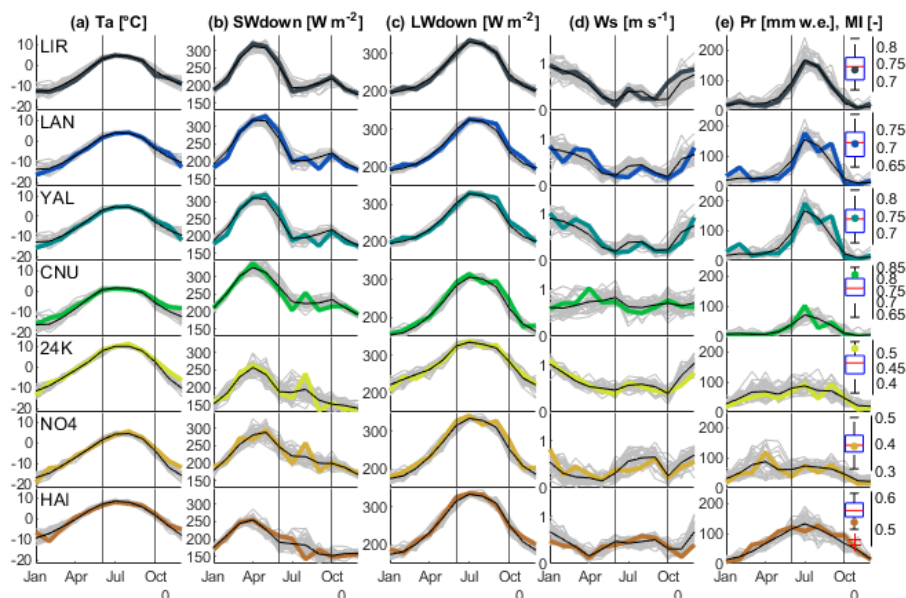


Figure 3. Monthly climatology derived from ERA5-Land for 1981-2019 (grey background lines), along with the monthly averages (black lines) and the study year at each glacier (colored lines). Plotted meteorological variables are **(a)** mean air temperature (T_a), **(b)** incoming shortwave radiation (SW_{\downarrow}), **(c)** incoming longwave radiation (LW_{\downarrow}), **(d)** wind speed (W_s) and **(e)** monthly precipitation sums (Pr). Black vertical lines indicate the average region-wide monsoon season. Boxplots show the monsoon index (MI) over ERA5-Land period as the fraction of monsoonal (June-September) to annual precipitation, with the colored dot indicating the value for the study year.

over the annual cycle with a clear maximum in July. A simple monsoon index (MI) is calculated for each year including the study year as the ratio between monsoon precipitation and annual average precipitation (Figure 3e). This value tends to be higher in the Central Himalaya compared to the sites on the South-Eastern Tibetan Plateau.

The yearly cycle of wind speeds (Figure 3d) varies considerably between sites. Common characteristics for most sites (except for Changri Nup) are that wind speeds are highest around December/January and that monsoonal wind speeds are generally higher than during the shoulder seasons.

At each site, we define the onset and recession date of monsoon based on visual inspection of the AWS records, observing the seasonal shift of air temperature, relative humidity, and longwave and shortwave radiation. For this, we define the date after which clear shifts are observable in the variables' regime (Figures A1 to A7).



155 3 Methods

3.1 Tethys-Chloris energy balance model

We use the hydrological, snow and ice modules of the Tethys-Chloris (T&C) land surface model (Fatichi et al., 2012; Mastrotheodoros et al., 2020; Paschalis et al., 2018; Botter et al., 2020) to simulate the mass and energy balance of the seven study glaciers. T&C simulates, in a fully distributed manner, the energy and mass budgets of a large range of possible land surfaces, including vegetated land, bare ground, water, snow and ice. Here, we apply the model at the point scale of the AWS locations to simulate the energy fluxes of the underlying surface and subsurface, which can comprise snow, ice and supraglacial debris cover layers, according to the local and dynamic conditions. The melt and accumulation of ice and snow, and the ice melt under debris are also explicitly simulated. The surface energy balances for the three different possible surfaces are for snow,

$$R_n(T_{sno}) + Q_v(T_{sno}) + Q_{fm}(T_{sno}) - H(T_{sno}) - \lambda E(T_{sno}) - G(T_{sno}) - dQ(T_{sno}) = 0, \quad (1)$$

165 for debris cover,

$$R_n(T_{deb}) + Q_v(T_{deb}) - H(T_{deb}) - \lambda E(T_{deb}) - G(T_{deb}) = 0, \quad (2)$$

and for ice,

$$R_n(T_{ice}) + Q_v(T_{ice}) - H(T_{ice}) - \lambda E(T_{ice}) - G(T_{ice}) - dQ(T_{ice}) = 0, \quad (3)$$

where $R_n [W m^{-2}]$ is the net radiation absorbed by the snow/debris/ice surface, $Q_v [W m^{-2}]$ is the energy advected from precipitation, $Q_{fm} [W m^{-2}]$ is the energy gained or released by melting or refreezing the frozen or liquid water that is held inside the snow pack, $H [W m^{-2}]$ is the sensible energy flux and $\lambda E [W m^{-2}]$ the latent energy flux for any of the surfaces, and $G [W m^{-2}]$ is the conductive energy flux from the surface to the subsurface. In ice, the conduction of energy is represented in the model down to a depth of 2 m after which it is assumed the ice pack is isothermal. Finally, $dQ [W m^{-2}]$ is the net energy input to the snow or ice pack. For debris on top of ice, and snow on top of debris or ice, the in-/outgoing fluxes towards/from the ice are adjusted according to the respective interface type. The sign convention is such that fluxes are positive when directed towards the surface. To close the energy balance, a prognostic temperature for the different surface types (T_{sno} , T_{deb} , T_{ice}) is estimated for each computational element. Iterative numerical methods are used to solve the non-linear energy budget equation until convergence for the ice and snow surface, and the heat diffusion equation for the debris surface, while concurrently computing the mass fluxes resulting from snow and ice melt and sublimation.

180

3.1.1 Radiative fluxes

R_n is calculated as the sum of incoming and outgoing shortwave and longwave fluxes as

$$R_n = SW_{\downarrow}(1 - \alpha) + LW_{\downarrow} + LW_{\uparrow}, \quad (4)$$



185 where SW_{\downarrow} [$W m^{-2}$] is the incoming shortwave radiation, $\alpha[-]$ is the surface albedo, LW_{\downarrow} [$W m^{-2}$] and LW_{\uparrow} [$W m^{-2}$] are the incoming atmospheric and outgoing longwave radiation components, respectively. In this study α is given as an input to the model based on the AWS observations. We prescribe α for all surface types as the daily cumulated albedo, which is the 24 hour sum of SW_{\uparrow} divided by the sum of SW_{\downarrow} centred over the time of observation (van den Broeke et al., 2004).

3.1.2 Incoming energy with precipitation

190 For calculating the incoming energy with precipitation, rain is assumed to fall at air temperature (T_a) when positive, with a lower boundary of $0^{\circ}C$. Snow is assumed to fall at negative T_a with an upper boundary of $0^{\circ}C$. Here, Q_v is the energy required to equalize the precipitation temperature with the surface temperature T_s and is therefore calculated as

$$Q_v = c_w P_{r,liq} \rho_w [\max(T_a, 0) - T_s] + c_i P_{r,sno} \rho_w [\min(T_a, 0) - T_s], \quad (5)$$

where $c_w = 4196 [J kg^{-1} K^{-1}]$ is the specific heat of water, $c_i = 2093 [J kg^{-1} K^{-1}]$ the specific heat of ice, $\rho_w = 1000 [kg m^{-3}]$ is the density of water and $P_{r,liq} [mm]$, $P_{r,sno} [mm]$ are the rain- and snowfall intensities, respectively.

3.1.3 Phase changes in the snow pack

The snow pack has a water holding capacity Sp_{wc} described in section 3.2.2. The energy flux gained/released by melting/refreezing the frozen/liquid water that is held inside the snow pack is calculated as:

$$Q_{fm}(t) = \begin{cases} f_{sp} \frac{\lambda_f \rho_w Sp_{wc}(t-dt)}{1000 dt}, & T_{sno}(t) < 0 \text{ and } T_{sno}(t-dt) \geq 0 \\ f_{sp} - \frac{\lambda_f \rho_w Sp_{wc}(t-dt)}{1000 dt}, & T_{sno}(t) \geq 0 \text{ and } T_{sno}(t-dt) < 0 \end{cases} \quad (6)$$

200 where $f_{sp} = \frac{5}{SWE} [m^{-1}]$ with $\max(f_{sp}) = 1$ is the fraction of the snowpack water equivalent ($SWE [mm w.e.]$) involved in either melting or freezing. This choice was made in order to mimic refreezing in the upper portion of the snowpack, while the snowpack is otherwise represented as a single layer. $\lambda_f = 333700 [J kg^{-1}]$ is the latent energy of melting and freezing of water, t stands for time, $dt [s]$ is the timestep, and the unit for T_{sno} is [$^{\circ}C$].

3.1.4 Turbulent energy fluxes

205 Over snow, debris and ice surfaces, the sensible energy flux is calculated as

$$H = \rho_a C_p \frac{(T_s - T_a)}{r_{ah}}, \quad (7)$$

where $T_s [^{\circ}C]$ is the surface temperature (generalised term for $T_{sno}, T_{deb}, T_{ice}$), $C_p = 1005 + [(T_a + 23.15)^2] / 3364 [J kg^{-1} K^{-1}]$ is the specific heat of air at constant pressure, $\rho_a [kg m^{-3}]$ is the density of air. The aerodynamic resistance $r_{ah} [s m^{-1}]$, which is also a function of wind speed (Ws) is calculated using the simplified solution of the Monin-Obokhov similarity theory (Mascart et al., 1995; Noilhan and Mahfouf, 1996). The roughness lengths of heat ($z_{0h} [m]$) and water vapour ($z_{0w} [m]$) used in the calculation of the aerodynamic resistance are equal in T&C ($z_{0h} = z_{0w}$), and ($z_{0h} = z_{0w} = 0.1 z_{0m}$). The roughness length



of momentum (z_{0m}) is set to 0.001 m for snow and ice surfaces (Brock et al., 2000), while we optimize it against the surface temperature for debris (see section 3.3).

215 Correct estimates of the latent energy flux due to water phase changes at the surface are important to accurately model glacier melt, especially under moist conditions (Sakai et al., 2004). Phase changes between the water and gas phase and the resulting energy fluxes are considered over all surfaces. The latent energy is limited by the availability of water in the form of ice and snow, or in the case of a debris surface, by the amount of water intercepted (interception storage capacity is set to 2mm). The latent energy flux is estimated from:

$$220 \quad \lambda E = \lambda_s \frac{\rho_a (q_{sat}(T_s) - q_a)}{r_{aw}}, \quad (8)$$

where λ_s is the latent energy of sublimation defined as $\lambda_s = \lambda + \lambda_f$, with $\lambda = 1000(2501.3 - 2.361T_a) [J kg^{-1}]$ as the latent energy of vaporisation. q_{sat} is the surface specific humidity at saturation at T_s , q_a is the specific humidity of air at the measurement height and r_{aw} the aerodynamic resistance to the vapour flux, which we assume equals r_{ah} .

3.1.5 Ground energy flux

225 The definition of the ground energy flux $G [W m^{-2}]$ differs based on the surface type. In the case of snow, it is equal to the energy transferred from the snowpack to the underlying ice or debris surface, where in the assumption of a slowly changing process, G can be approximated with the temperature difference of the previous time step ($t-1$), which allows to solve for G outside the numerical iteration to find the snow surface temperature of the current time step:

$$G_{sno}(t) = k_{sno} \frac{T_{sno}(t-1) - T_{deb,ice}(t-1)}{d_{sno}} \quad (9)$$

230 where $k_{sno} [W K^{-1} m^{-1}]$ is the thermal conductivity of snow and $d_{sno} [m]$ is the snow depth. For ice in the absence of snow and debris, it is the energy flux from the ice pack to the underlying surface or to the ice at a depth of 2m:

$$G_{ice}(t) = k_{ice} \frac{T_{ice}(t-1) - T_{grd}(t-1)}{d_{ice}} \quad (10)$$

where $k_{ice} [W K^{-1} m^{-1}]$ is the thermal conductivity of ice, $T_{grd} [^{\circ}C]$ is the temperature of the underlying ice, and $d_{ice} [m]$ is the relevant ice thickness. For debris, which was discretised into eight layers at all debris-covered sites, G is the energy flux
 235 conducted into the debris layers. Its calculation is for a given time t and depth z

$$G(z, t) = -k_d \frac{\partial T_{deb}(z, t)}{\partial z_d}, \quad (11)$$

where $k_d [W K^{-1} m^{-1}]$ is the debris thermal conductivity (see section 3.3) and $T_{deb}(z, t) [^{\circ}C]$ is the debris temperature at time t and depth z . $G(z, t)$ can be included in the heat diffusion equation as such:

$$cv_s \frac{\partial T_{deb}(z, t)}{\partial t} = \frac{\partial}{\partial z_d} (-G(z, t)), \quad (12)$$



240 where cv_d is the debris heat capacity. Under the assumption of homogeneous debris layers, $\kappa [m^2 s^{-1}]$ as the debris heat diffusivity replaces the term $\frac{k_d}{cv_s}$ and equation (12) can be written as:

$$\frac{\partial T_{deb}(z,t)}{\partial t} = \kappa \frac{\partial^2 T_{deb}(z,t)}{\partial z^2}, \quad (13)$$

The heat diffusion equation (13) is solved using iterative numerical methods. This way, the debris temperature profile $T_{deb}(z,t)$ is solved together with $G(z,t)$ at any depth and time. The conductive energy flux at the base of the debris is used to
245 heat the ice and to calculate ice melt once above the melting point.

3.2 Mass balance in T&C

3.2.1 Precipitation partition

Input precipitation is required to be partitioned into solid Pr_{sno} and liquid Pr_{liq} precipitation, because of the differing impacts of snow and rain on the energy and mass balance. For this study, the precipitation partition method described by Ding et al.
250 (2014) was implemented into T&C. This parameterisation has been developed specifically for High Mountain Asia based on a large dataset of rain, sleet and snow observations, and does not require recalibration. It determines the precipitation partition based on the wet-bulb temperature, station elevation and relative humidity and allows for sleet events, as a mixture between liquid and solid precipitation. Ding et al. (2014) found the wet-bulb (T_{wb}) to be a better predictor than T_a of the precipitation type, that the temperature threshold between snow and rain increases at higher elevations, and that the probability of sleet is
255 reduced in conditions of low relative humidity.

3.2.2 Water content of the snow, ice and debris layers

The water content of ice is approximated with a linear reservoir model. The liquid water outflow is proportional to the ice pack water content $Ip_{wc} [mm w.e.]$, which is initiated when Ip_{wc} exceeds a threshold capacity, prescribed as 1% of the ice water equivalent ($IWE [mm w.e.]$). The Ip_{wc} is the sum of ice melt and liquid precipitation, minus the water released from the ice
260 pack. The water released is the sum of the ice pack excess water content plus the outflow from the linear reservoir, given as $I_{out} = Ip_{wc}/K_{ice}$, where K_{ice} is the reservoir constant which is proportional to the ice pack water equivalent. Unlike within snow packs, Q_{fm} is not accounted for within the ice pack, since water is presumed to be evacuated quickly from the ice due to runoff without refreezing.

The water content of the snow pack $Sp_{wc} [mm w.e.]$ is approximated using a bucket model, in which outflow of water from
265 the snow pack occurs when the maximum holding capacity of the snow pack is exceeded. Following the method of Bélair et al. (2003), the maximum holding capacity of the snow pack is based on SWE , a holding capacity coefficient and ρ_{sno} . Snowmelt plus liquid precipitation, minus the water released from the snow pack gives the current Sp_{wc} . If T_{sno} is greater than $0^\circ C$ then the snow pack water content is assumed to be liquid, whereas otherwise it is assumed frozen.

For supraglacial debris, both observations and methods for modelling its water content are lacking. We thus use a simplified



270 scheme for accounting for moisture at the surface of the debris, in order to mimic the drying process of the debris surface:
we assume debris to have a dynamic interception storage, which can hold a maximum of 2 mm water at all debris-covered
sites and can be refilled by snowmelt or liquid precipitation. The evaporative flux from the debris and the latent energy flux of
evaporation is therefore limited by this interception storage.

275 3.2.3 Glacier mass balance

The mass balance calculation of snow and ice is rather similar, so they will be described together here. Calculations are
performed for snow if there is snow precipitation during a timestep or the modelled SWE at the surface is greater than zero.
Net input of energy to the snow or ice pack will increase its temperature, and after the temperature has been raised to the
melting point, additional energy inputs will result in melt. The change in the average temperature of the ice or snowpack dT is
280 controlled using:

$$dT = \frac{dQ dt}{c_i \rho_w WE_b} 1000, \quad (14)$$

Where dt is the time step [h] and WE_b [mm w.e.] is IWE or SWE before melting and limited to a maximum of 2000 mm,
assumed to be the water equivalent mass exchanging energy with the surface. Energy inputs into an iso-thermal ice/snow pack
result in melt M [mm w.e.] as

$$285 M = \frac{dQ dt}{\lambda_f \rho_w} 1000 \quad (15)$$

The water equivalent mass of the snow/ice pack after melting $WE(t)$ [mm w.e.] is updated conserving the mass balance
following:

$$WE(t) = WE(t - dt) + Pr_{sno}(t) - E(t) dt - M(t), \quad (16)$$

Here $E = \lambda E / \lambda_s$ [mm] is the sublimation from ice and snow. The snow density is assumed to be constant with depth and cal-
290 culations are performed assuming one single snow pack layer. The snow density evolves over time using the method proposed
by Verseghy (1991) and improved by Bélair et al. (2003). In this parameterisation the snow density increases exponentially
over time due to gravitational settling and is updated when fresh snow is added to the snowpack. Two parameters are required
in this scheme, ρ_{sno}^{M1} and ρ_{sno}^{M2} [$kg m^{-3}$], which represent the maximum snow density under melting and freezing conditions,
respectively. The depth of the ice pack can be increased through the formation of ice from the snow pack (ice accumulation),
295 which is prescribed to occur if the snow density increases to greater than $500 kg m^{-3}$ (a density associated with the firm to ice
transition) and at a rate of $0.037 mm h^{-1}$ (Cuffey and Paterson, 2010). The density of ice is assumed constant with depth and
equal to $916.2 kg m^{-3}$.

3.3 Debris parameters

A major challenge in physically based mass-balance modelling of debris-covered glaciers is the assignment of appropriate
300 debris properties. Besides the debris thickness, which was measured at the AWS location, the thermal conductivity k_d , the



roughness length z_0 of the debris surface, the surface emissivity ϵ_d , the debris volumetric heat capacity cv_d and the debris density ρ_d have to be assigned. While the latter three can be quantified using literature values, there is more uncertainty about k_d and z_0 , two highly variable quantities that are difficult to measure in the field, but which EB models are highly sensitive to. We thus choose to optimize them, since our primary requirement is an accurate representation of the energy and mass balance:

305 (1) in a first step, we optimize k_d simulating only the conduction of energy through the debris during snow free conditions, with the LW_{\uparrow} -derived surface temperature $T_{s,LW}$ as an input, the ice melt as the target variable and the Nash-Sutcliffe Efficiency $NSE[-]$ as performance metric. (2) Next, we run the whole energy balance model and optimize z_0 for snow-free conditions, with all required meteorological inputs, and the optimal k_d from step (1), while comparing modelled T_s against $T_{s,LW}$, using NSE as performance metric. The resulting parameters are given in Table 3.

310 3.4 Uncertainty estimation

We calculate the uncertainty associated with all energy and mass balance components by performing 10^3 Monte Carlo simulations for each study site at the AWS location. We vary three debris parameters (k_d, z_{0m}, ϵ_d), debris thickness h_d , as well as six measured model input variables: air temperature T_a , the vapor pressure at reference height $ea[-]$, SW_{\uparrow} , SW_{\downarrow} , LW_{\downarrow} , the total precipitation before partition Pr , and the wind speed W_s . Measured outgoing shortwave radiation SW_{\uparrow} was included into the

315 Monte Carlo set, as it determines our input α , as discussed in Section 3.1.1. While the parameter uncertainty range was defined based on previously published values for debris (e.g. Yang et al., 2017; Rounce et al., 2015; Evatt et al., 2015; Reid and Brock, 2010; Nicholson and Benn, 2006; Rowan et al., 2020; Lejeune et al., 2013; Collier et al., 2015; McCarthy, 2018), the debris thickness measurement uncertainty was given with a range of $1cm$ and the range for the meteorological inputs was set based on the respective sensor uncertainties (see Table 4). All uncertainties were equally distributed around the standard parameter

320 values and observations. Uncertainties are given as one standard deviation of the error of the Monte Carlo runs against the standard run.

Table 3. Debris parameter values for each site derived from the two-step optimization procedure.

	Lirung	Langtang	Changri Nup	24K	Hailuogou
$k_d [W m^{-1} K^{-1}]$	1.09	1.65	1.77	1.45	0.72
$z_{0m} [m]$	0.7	0.38	0.11	0.15	0.027

4 Results

4.1 Modelled mass balance

The model accurately reproduces the measured surface height change (ablation and accumulation) at both debris-covered and

325 clean-ice glaciers (Figure 4). The maximum uncertainties associated with each model output ranges from $\pm 4\%$ (Parlung No.4, Figure 4f) to $\pm 15\%$ (Yala, Figure 4c). Where Ultrasonic Depth Gauge (UDG) records are available (Lirung, Langtang, Yala,



Table 4. Uncertainty ranges of parameters and input variables used for Monte Carlo runs. Where units are indicated with [-], the parameter or variable was perturbed by the fractional value shown.

Parameter/ Variable	Range	Parameter/ Variable	Range
k_d [-]	± 0.1	SW_{\downarrow} [-]	± 0.03
z_0 [-]	± 0.1	SW_{\uparrow} [-]	± 0.03
ϵ_d [-]	± 0.05	LW_{\downarrow} [-]	± 0.03
h_d [mm]	± 5	Pr [-]	± 0.15
Ta [$^{\circ}C$]	± 0.2	W_s [m/s]	± 0.3
ea [-]	± 0.02		

Changri Nup), the deviations of the simulations from the observations stay within the uncertainty range (Figure 4a-d). We decided to not consider the UDG record from Changri Nup after a large August snowfall, as variables describing the surface state (e.g. α , LW_{\uparrow}) following this event indicate a discontinuous snow cover at the AWS location, while the UDG, which is
 330 some meters away from the AWS, shows continuous snow cover with depths at the order of tens of centimeters. This discrepancy was also confirmed by observation of the site from October 2016. It was thus not possible to match the UDG record with our model for the late ablation period on Changri Nup, but our model closely reproduces observed surface height change for the pre-monsoon and early monsoon (Figure 4d), when AWS and UDG observations agree in terms of surface state. The deviation to measured melt is larger than the uncertainty range at 24K and Parlung No.4 for two and one individual stake
 335 readings, respectively, but the overall agreement is very good also at these sites (Figure 4e,f). For Parlung No.4 there are no stake measurements available before July 21 due to the long-lasting snow cover.

Mass losses over the ablation seasons (combining ice melt, snow melt and sublimation) show considerable variability between study sites and over time at each site: At all sites, ice melt is the dominant mass loss component, accounting for 65.8% (Changri Nup, Figure 5c) to 95.4% (Hailuogou, Figure 5g) of the total mass losses. It increases initially during premonsoon at all sites,
 340 then tends to plateau at Lirung and Langtang. Snow melt is a smaller component of mass loss, accounting for 0.1% (24K, Figure 5e) to 33.1% (Hailuogou, Figure 5g) of the total mass losses. However, it is an important control of both amounts and patterns of ice melt, as ice melt rates are suppressed during periods of snow cover (Figure 5). A longlasting pre-monsoonal snowpack can delay the onset of ice melt, as at Parlung No.4, where ice melt is delayed until the end of June (Figure 5f). Similarly, intermittent snow cover protects the ice from melting at the two highest sites (Yala and Changri Nup) during the summer
 345 months (Figure 5c and d). Sublimation from ice and snow represents a very small share of the total mass losses, and ranges from 0.01% (Lirung, Figure 5a) to 1.2% (Changri Nup, Figure 5d). It mostly occurs under dry conditions during premonsoon at the highest sites (Changri Nup, Yala). Debris cover is clearly another important control of total mass losses: The presence

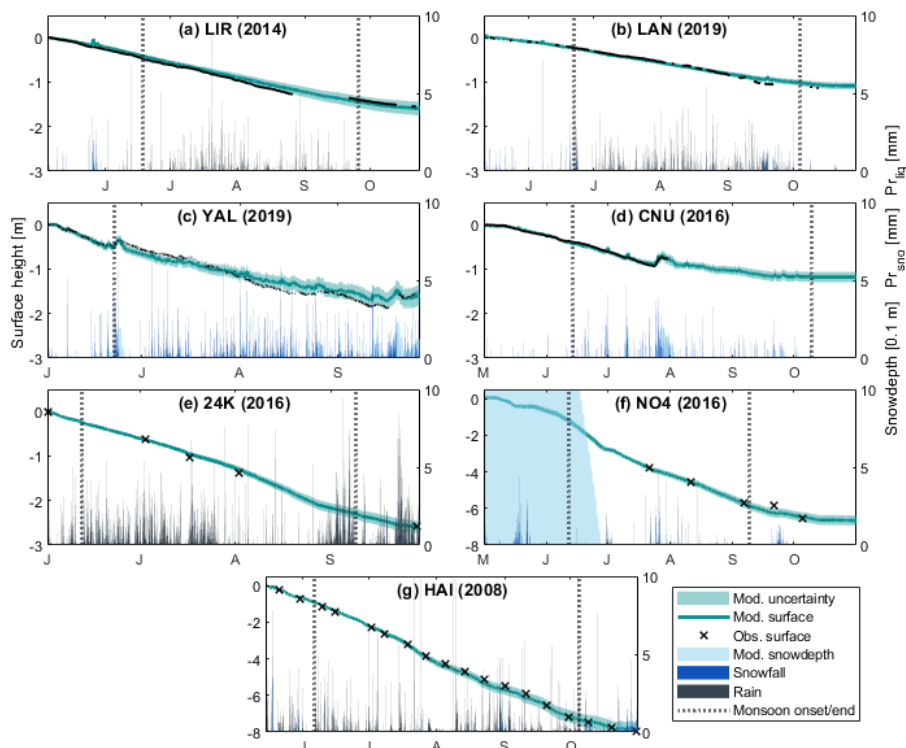


Figure 4. (a)-(g) Measured vs. modelled surface change at all study sites, including ice melt, snow melt, sublimation, precipitation phase and snow depth. Measured melt is either from ablation stakes (black circles) or Ultrasonic Depth Gauges (black lines). Vertical dotted lines indicate monsoon onset and end.

of debris at least 10 cm thick (Changri Nup, Lirung, Langtang and 24K) causes average melt rates to be comparatively low (8.2, 8.5, 6.1 and 19.4 $mm d^{-1}$, Figure 5a,b,d and e), while at the 'dirty-ice' site (Hailuogou, with thin and patchy debris, approximated to be 1 cm), the melt rate is higher (42.7 $mm d^{-1}$, Figure 5g) over the simulation period, peaking in mid-July. Relatively high average melt rates are also reached at the clean ice sites Parlung No.4 (34.6 $mm d^{-1}$, Figure 5f) and Yala (16.6 $mm d^{-1}$, Figure 5c), despite the high altitude of the latter.

355 4.2 Modelled energy balance

The main energy source on all glaciers and during all seasons is SW_{net} (Figure 6). At all sites and over the entire modelling period, LW_{out} is the largest energy sink, but it remains comparably stable in magnitude between the seasons (Figure A8). The turbulent heat fluxes (H and LE), and dQ (G on debris) act as energy sinks on average at all sites. G can however act in both ways, as an energy source when warming the glacier, and as an energy sink when warming the air. In our definition G sums

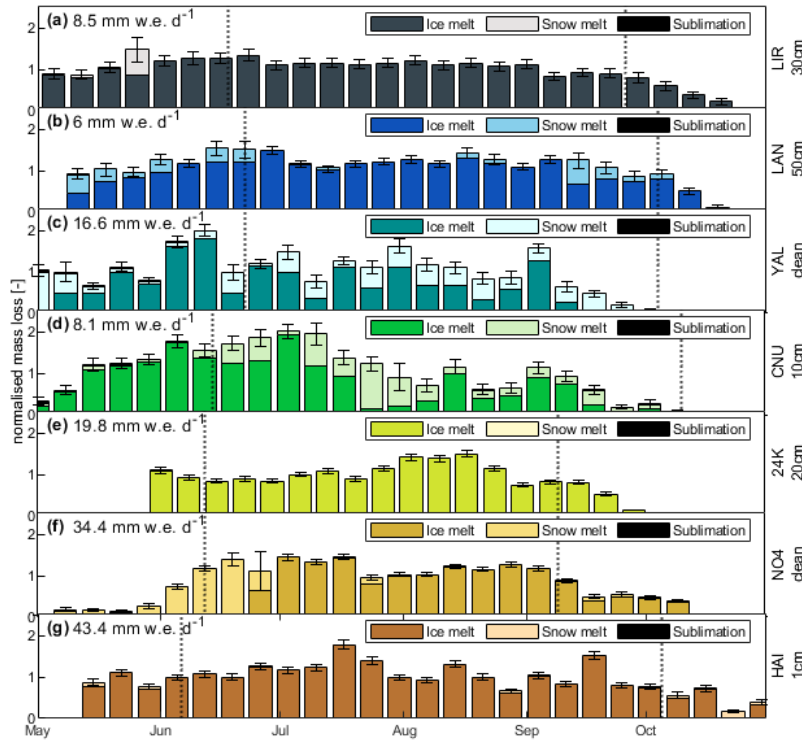


Figure 5. (a)-(g) Melt rates of ice and snow (stacked) as weekly averages at each site. Vertical dotted lines indicate monsoon onset and end. Error bars depict the uncertainty (standard deviation) of the estimates. Melt rates are normalized to the mean of the ice melt over the entire period (value in the upper left of each panel).

360 up all types of conductive energy fluxes in the snow-debris-ice column. Part of the energy is used for heating the snow, ice or debris-ice surface layer until melt occurs (dG , Table 5). The relative contributions of the individual sinks strongly depends on the surface type: LW_{net} is an important sink at the clean-ice sites, while the turbulent fluxes remain small there. On the debris-covered glaciers with debris >10 cm thick, where LW_{net} plays a relatively small role, the turbulent fluxes act as major energy sink. Where debris is thin, they instead act as additional energy sources.

365 In the following, we consider how energy fluxes change when moving from pre-monsoon to monsoon. Note that the sign of this change depends on the sign of the original flux, which is negative when the flux acts as an energy sink (energy away from the surface) and positive when the flux acts as a source (energy towards the surface). As an example, a negative change in LE , when acting as a sink, means an increase in its magnitude.

The seasonal imprint of the monsoon on the energy balance is very clear at all study sites on average and diurnally: There is a strong reduction in the magnitude of SW_{\downarrow} during monsoon across sites (with decreases ranging between -41.8 and $-135 W m^{-2}$ at the seven sites, Figure 7 and Table 5), which however remains the main energy source. SW_{\uparrow} , which is a sink controlled by surface albedo, follows these changes (ranging from $+5.4$ to $+164.8 W m^{-2}$ between sites) with the exception



of Changri Nup, where SW_{\uparrow} increases in magnitude (by $-12.1 W m^{-2}$, Table 5) as a consequence of ephemeral snow cover (Figure 4). LW_{\downarrow} on the other hand increases at all sites (by $+15.7$ to $+57.0 W m^{-2}$), and LW_{\uparrow} slightly increases in magnitude
375 as well (by -1.0 to $-13.3 W m^{-2}$) (Figure 7 and Table 5).

At the debris-covered sites, the reduction in R_{net} from pre-monsoon to monsoon is balanced by a reduction in the magnitude of H (with changes of $+15.6$ to $+67.7 W m^{-2}$ between sites), which acts as a major energy sink during both sub-seasons (Figure 6, 7 and Table 5). LE , which plays a small role as a sink compared to H during pre-monsoon, increases in magnitude at the debris-covered sites (with changes ranging from -2.7 to $-24.4 W m^{-2}$, Figure 7 and Table 5), and acts as a considerable heat
380 sink during the monsoon. As a result of these contrasting changes, dQ remains fairly similar between the pre-monsoon and monsoon at the debris covered sites (with changes ranging between $+1.3$ and $-3.3 W m^{-2}$) (Figure 7a,c,e,g and Table 5). This is partly a consequence of a compensation between increased/reduced melt rates before/after noon (Figure A10). An exception is the thin-debris site Hailuogou, where dQ increases in magnitude (by $-26.2 W m^{-2}$), mostly as a result of warmer nights (Figure A10).

385 At the clean-ice sites, LW_{\uparrow} is initially larger than LW_{\downarrow} in the pre-monsoon, but the two become almost equal while adjusting to monsoon conditions, causing the LW_{net} to be close to zero (LW_{\downarrow} : $+40.7$ to $+57.0 W m^{-2}$, and LW_{\uparrow} : -3.1 to $-11.7 W m^{-2}$), Table 5 and Figure 6c and f). LE switches sign when moving from pre-monsoon to monsoon, becoming a small condensation energy flux (Yala: 0.1 , Parlung No.4: $3.8 W m^{-2}$). So does H at Yala, becoming a small heat source instead of a heat sink ($0.5 W m^{-2}$, Table 5), while at Parlung No.4, H is a heat source across the seasons (pre-monsoon: $4.9 W m^{-2}$, monsoon:
390 $12.7 W m^{-2}$, Table 5). The turbulent fluxes, however, remain comparably small in magnitude at the clean ice sites (Figure 6c and f). dQ increases in magnitude at Parlung No.4 from pre-monsoon to monsoon (by $-131.0 W m^{-2}$) and decreases in magnitude at Yala (by $-10.2 W m^{-2}$) (Figure 7b and d). Both changes are consequences of snow cover, prevalent during pre-monsoon at Parlung No.4 and during monsoon at Yala (Figure 4c and f).

Hailuogou, our 'dirty ice glacier', behaves entirely differently compared to both debris-covered and clean sites, with the turbu-
395 lent energy fluxes increasing in magnitude to become considerable heat sources during monsoon (H : $+15.6 W m^{-2}$ and LE :, $+24.5 W m^{-2}$), driving a pronounced increase in the energy available for melt (dQ : $-26.2 W m^{-2}$, Figure 6, 7 and Table 5).

4.3 Turbulent fluxes at debris-covered sites and their controls

The turbulent fluxes LE and H are important heat sinks on debris-covered glaciers and heat sources on the dirty-ice glacier, while they remain small on the clean-ice glaciers (Figure 6). Their magnitude largely determines the energy that is conducted
400 into the debris and used for ice melt. We observe a decrease in the magnitude of H and an increase in the magnitude of LE going from pre-monsoon to monsoon at the debris-covered glaciers, while both increase as sources of energy at the dirty ice glacier (Figure 7).

The predictive power of the temperature gradient between surface and air $gT [^{\circ}C^{-1}]$ and W_s as well as their combination for
405 determining H and LE were assessed using a univariate polynomial regression model for the single predictors and a multiple polynomial regression model using both variables, and both models had 2 degrees of freedom. H is largely controlled by the



temperature gradient between surface and air (g_T) on debris-covered glaciers, which explains between 75 and 99% of the variability of H (Figure A9), and g_T decreases during monsoonal conditions by -0.05 to -1.44 $^{\circ}\text{C m}^{-1}$ (Table 6). Here it is clear that a smaller temperature gradient between surface and air during the monsoon reduces the magnitude of H as a
410 sink. Wind emerges as the most important control of H at the dirty-ice glacier, explaining up to 89% of variability (Figure A9). The mean magnitude of W_s increases at that site from 1.23 m s^{-1} in pre-monsoon to 2.10 m s^{-1} in monsoon (Table 6). A cold surface in combination with a wind-enhanced turbulence and fast turnover of warm air mass results in H becoming a potent heat source on the dirty-ice glacier. From a physical perspective, the same holds for clean-ice glaciers experiencing simultaneously high wind speeds and high air temperatures. This is, however, not observed on Yala and Parlung No.4, where
415 air temperatures stay comparably low and average wind speed decreases slightly in monsoon compared to pre-monsoon (Table 6).

Neither RH , g_T , or W_s on their own explain the variability of LE across sites (Figure A9). LE however increases consistently from pre-monsoon to monsoon together with an increase in the duration of moisture availability at the surface of debris-covered glaciers (by 21 to 63%, Table 6). In fact, evaporation and the related LE release tends to be water-limited during pre-monsoon,
420 but energy-limited during monsoon (Figure 8). This implies that the availability of moisture is driving the increase of LE from pre-monsoon to monsoon. However, on the dirty-ice glacier, LE acts as a heat source across sub-seasons and switches sign during monsoon at the clean-ice sites. This happens when T_a is consistently higher than T_s , causing condensation when the warm air touches the cold glacier-, or thin debris-surface.

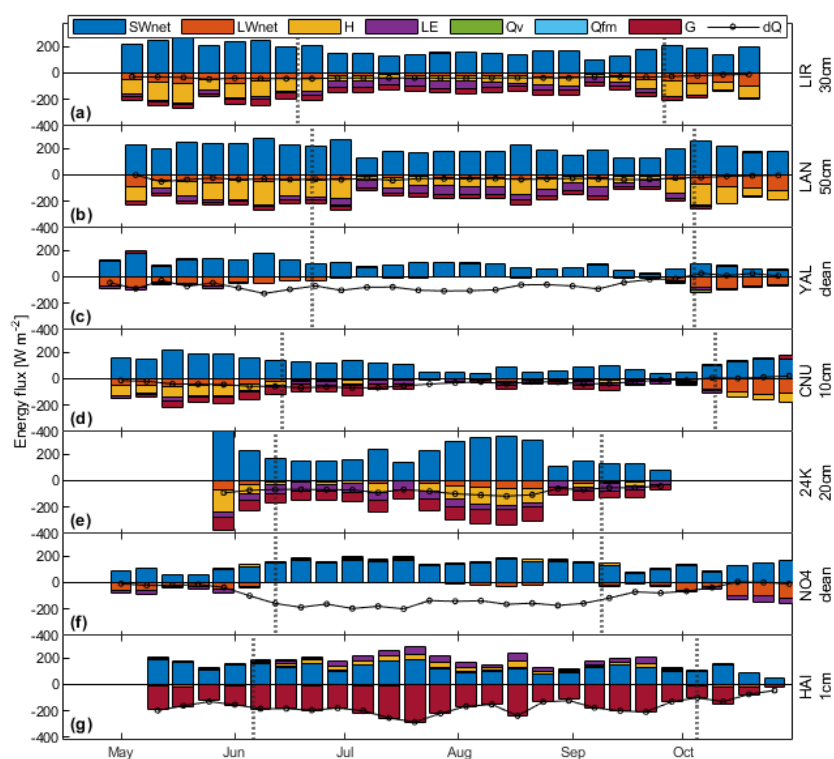


Figure 6. (a)-(g) Stacked energy fluxes weekly averages at each site, depicting the components SW_{net} , LW_{net} , H , LE , Q_v , Q_{fm} , G and dQ . Energy fluxes are negative fluxes when directed away from the surface and positive when directed towards the surface.



Table 5. Mean energy balance components at each site and for pre-monsoon (pre), monsoon (mon), and post-monsoon (post) periods, as well as flux magnitude changes from pre-monsoon to monsoon, and monsoon to post-monsoon. All values are in $W m^{-2}$.

	SWin			SWout			LWin			LWout			LE			
	pre	mon	post	pre	mon	post	pre	mon	post	pre	mon	post	pre	mon	post	
LJR	mean	277.1	170.0	224.1	-39.8	-21.1	-41.3	293.3	341.2	264.0	-358.1	-364.8	-340.4	-16.0	-40.4	-1.9
	Δ		-107.1	54.1	18.7	-20.2	47.9	-77.2			-6.7	24.4		-24.4	38.5	
LAN	mean	295.6	208.1	262.4	-55.9	-30.1	-48.6	292.3	334.7	238.6	-339.3	-352.8	-326.1	-26.4	-49.9	-5.8
	Δ		-87.5	54.3	25.7	-18.4	42.3	-96.0			-13.5	26.7		-23.5	44.1	
YAL	mean	307.7	172.7	271.8	-169.4	-94.4	-195.0	248.5	305.5	212.3	-299.8	-311.6	-287.1	-13.7	0.1	-12.2
	Δ		-135.0	99.1	75.0	-100.6	57.0	-93.2			-11.7	24.4		13.7	-12.3	
CNU	mean	237.1	154.7	258.1	-60.6	-72.7	-126.0	268.8	310.2	196.4	-318.7	-319.7	-300.4	-15.7	-18.1	-3.1
	Δ		-82.4	103.4	-12.1	-53.3	41.5	-113.8			-1.0	19.3		-2.5	15.0	
24K	mean	296.6	219.7	140.9	-18.5	-13.0	-8.3	324.6	349.3	336.6	-369.9	-371.3	-351.0	-50.6	-52.7	-40.0
	Δ		-76.9	-78.8	5.4	4.7	24.7	-12.7			-1.3	20.3		-2.1	12.7	
NO4	mean	308.5	209.1	197.3	-219.6	-54.8	-81.5	267.5	308.2	261.5	-310.3	-313.4	-310.5	-17.6	3.6	-18.5
	Δ		-99.5	-11.8	164.8	-26.7	40.7	-46.7			-3.1	2.9		21.2	-22.1	
HAI	mean	178.2	136.4	105.8	-25.2	-10.8	-28.4	314.6	330.3	273.1	-324.5	-327.9	-309.1	5.4	31.6	-4.8
	Δ		-41.8	-30.6	14.4	-17.6	15.7	-57.2			-3.4	18.8		26.2	-36.4	

	H			G			Qv			dQ			dG			
	pre	mon	post	pre	mon	post	pre	mon	post	pre	mon	post	pre	mon	post	
LJR	mean	-116.7	-48.4	-86.5	-33.7	-36.4	-18.7	0.0	0.0	0.0	-37.5	-36.5	-19.0	5.6	0.0	16.6
	Δ		68.3	-38.0	-2.7	17.8	0.0	0.0	0.0	0.0	1.0	17.5		-5.6	16.6	
LAN	mean	-126.7	-77.4	-111.4	-22.5	-26.2	-7.8	0.0	-0.3	0.0	-26.9	-28.7	-10.4	2.2	0.0	27.2
	Δ		49.3	-34.1	-3.7	18.4	-0.3	0.3			-1.8	18.4		-2.2	27.2	
YAL	mean	-2.3	0.5	1.4	4.7	0.9	0.0	0.0	-0.2	-4.1	-74.8	-64.6	-0.3	4.7	0.9	0.0
	Δ		2.8	0.9	-3.8	-0.9	-0.2	-3.9			10.2	64.3		-3.8	-0.9	
CNU	mean	-67.4	-8.7	-36.1	-39.2	-29.1	10.4	0.0	0.0	0.0	-34.6	-34.1	-0.2	17.8	2.1	10.7
	Δ		58.7	-27.4	10.1	39.5	0.0	0.0			0.5	33.9		-15.7	8.6	
24K	mean	-99.8	-50.8	-24.4	-81.8	-81.4	-53.1	-0.3	0.2	0.6	-79.5	-81.6	-53.7	0.3	0.0	0.0
	Δ		49.0	26.4	0.4	28.4	0.6	0.4			-2.1	27.9		-0.3	0.0	
NO4	mean	4.7	12.3	5.8	0.2	0.1	0.1	0.2	0.2	0.0	-32.3	-162.6	-54.1	0.2	0.1	0.0
	Δ		7.6	-6.6	-0.1	-0.1	0.0	-0.2			-130.4	108.5		-0.1	-0.1	
HAI	mean	9.1	25.7	-9.9	-150.4	-186.4	-16.5	1.2	1.9	0.1	-158.1	-186.8	-36.9	2.1	0.5	18.8
	Δ		16.6	-35.5	-35.9	169.9	0.7	-1.8			-28.7	149.9		-1.6	18.3	

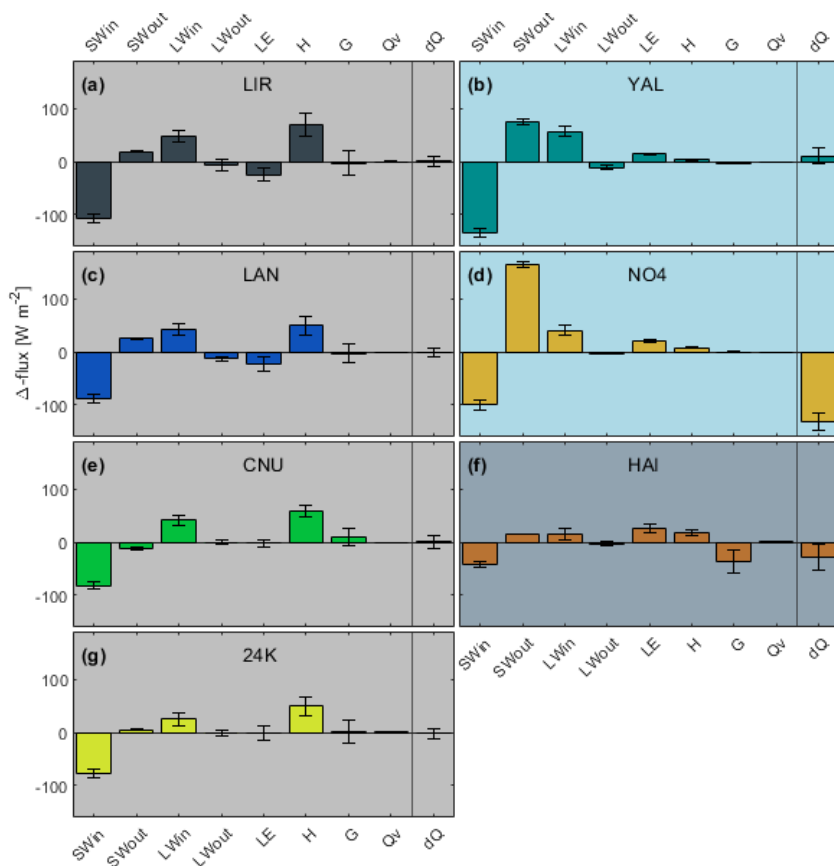


Figure 7. (a)-(g) Differences in energy balance components from pre-monsoon to monsoon at each site including their uncertainties (error bars). The direction of change is to be considered relative to the sign of the original flux (x-axis). For example, a positive change in a negative flux means a reduction in the flux, and can also lead to a change in sign. Background indicates the surface type of the site: grey indicates debris-covered, light blue indicates clean-ice sites, and grey-blue indicates thin-debris.

5 Discussion

425 5.1 Monsoon effects

Monsoon impacts on glaciers are complex and spatially variable along the Himalayan arc. The varying strength of the monsoons reflect in the distinct meteorological seasonality between our study sites (Figure 3). The ablation period occurs between April and November at all sites, and all sites are affected by the Indian and East Asian summer monsoons during this period (Figures A1 to A7). On average, 70 to 85% of precipitation arrives during the summer months (June-September) at our Central
 430 Himalayan sites (Lirung, Lantang, Yala and Changri Nup, Figure 3a-d) in contrast to 40 to 55% at the eastern sites (24K, Parlung No.4 and Hailuogou, Figure 3e-g).

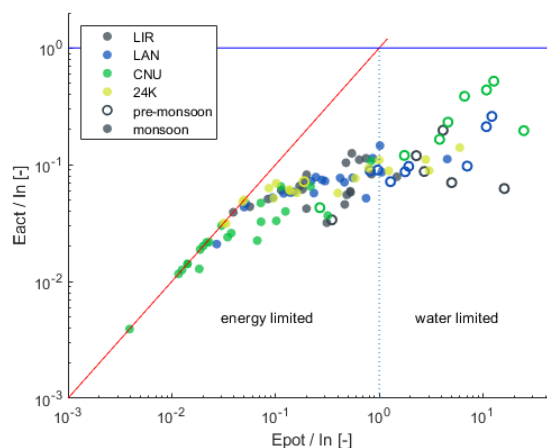


Figure 8. Budyko diagram with the 5-day mean potential evaporation rate during snow-free conditions (E_{pot}) relative to the mean available intercepted water (In) on the x-axis, and the actual evaporation rate during snow-free conditions (E_{act}) relative to In on the y-axis. Only debris-covered glaciers, where LE is a sink term on average, are shown.

Table 6. Mean cloud-cover fraction (ccf), relative humidity (RH), temperature gradient between surface and air (g_T), wind speed (Ws) and the percentage of time during which the debris is modelled to hold intercepted water (In) for each site and season, also indicating percent changes between the sub-seasons.

		ccf [-]			RH [%]			g_T [$^{\circ}C m^{-1}$]			Ws [$m s^{-1}$]			In [%]		
		pre	mon	post	pre	mon	post	pre	mon	post	pre	mon	post	pre	mon	post
LIR	mean	0.76	0.91	0.74	68.1	90.8	67.1	1.19	0.78	0.89	0.47	0.27	0.52	40.1	74.0	26.4
	Δ	0.14	-0.16		22.6	-23.6		-0.40	0.10		-0.19	0.24		33.9	-47.6	
LAN	mean	0.76	0.86	0.62	80.7	96.9	56.3	1.02	0.97	0.95	1.79	1.10	1.27	38.8	75.3	9.5
	Δ	0.10	-0.24		16.2	-40.6		-0.05	-0.02		-0.68	0.17		36.5	-65.8	
YAL	mean	0.65	0.87	0.55	69.8	93.0	39.4	-0.36	-0.96	-0.89	1.74	1.00	1.68	-	-	-
	Δ	0.21	-0.32		23.2	-53.6		-0.59	0.07		-0.74	0.67		-	-	
CNU	mean	0.78	0.89	0.58	71.2	89.2	39.3	1.69	0.25	0.89	1.88	1.09	2.48	16.2	79.3	5.3
	Δ	0.11	-0.31		18.1	-50.0		-1.44	0.64		-0.79	1.39		63.1	-74.0	
24K	mean	0.70	0.82	0.91	73.1	80.6	81.2	1.86	0.73	0.18	1.33	1.56	1.35	56.8	79.1	84.3
	Δ	0.12	0.08		7.4	0.7		-1.13	-0.55		0.22	-0.21		22.3	5.2	
NO4	mean	0.72	0.87	0.79	65.7	81.3	73.1	-0.78	-2.01	-0.62	2.96	2.67	3.23	-	-	-
	Δ	0.14	-0.07		15.7	-8.3		-1.22	1.39		-0.28	0.56		-	-	
HAI	mean	0.88	0.93	0.91	81.3	92.3	90.6	-2.08	-2.61	0.38	1.23	2.15	0.93	99.8	100.0	75.6
	Δ	0.05	-0.01		10.9	-1.6		-0.53	2.99		0.91	-1.22		0.2	-24.4	

5.1.1 All glaciers

Overcast conditions caused by monsoon increase LW_{\downarrow} and with that the magnitude of T_a at all sites (Figures 6 and 7). SW_{\downarrow} on the other hand is reduced at all glacier surfaces due to the reflection and scattering of persistent, heavy clouds. While the



435 changes of these two primary sources of energy partly counteract each other in terms of energy supply to glacier surfaces during monsoon, we find that net incoming radiation decreases in magnitude everywhere. Another major control on the energy and mass balance of all glaciers are the snowcover dynamics, which in turn are driven by the precipitation seasonality and the partition of precipitation into rain and snow. For example, in the case of Parlung No.4, the onset of glacier melt was delayed until well after monsoon onset, until all snow had disappeared (Figure 5). After snow has melted out, ephemeral snowcover from
440 monsoonal precipitation increases surface albedo and raises SW_{\uparrow} , protecting the ice and suppressing melt rates throughout the summer. This is especially relevant at high elevation sites (Yala, Changri Nup). An interruption of the monsoon at 24K occurred in August 2016, possibly associated with an El Niño event (Kumar et al., 2006). During this interruption the energy balance returned to a pre-monsoonal regime of clearer skies, more pronounced diurnal temperature amplitudes, low precipitation rates and lower relative humidity (Figure A5), resulting in higher melt rates during that period (Figure 6e). Our analysis shows that
445 some effects of monsoon are common for all surface types, while the presence or absence of debris and its thickness control how the incoming energy is absorbed and transmitted to the ice.

5.1.2 Debris-covered glaciers

Monsoon conditions in combination with debris cover affects the energy balance in a way that stabilizes melt rates over the ablation period, despite increasing air temperatures typical of monsoon (Figure 6). Enhanced melt during the night and morning
450 in monsoon, resulting from higher T_a , is partly offset during the cooler afternoon hours (Figure A10) when the wet air masses usually arrive in this region, bringing intense cloud-cover and precipitation. While H decreases as a consequence of a smaller average temperature gradient between surface and air, more latent energy is released from the wet debris surface, which shifts from a water-limited process during pre-monsoon to an energy-limited process during monsoon (Figure 8). It has been known from studies at individual sites that debris cover protects the ice by returning energy to the atmosphere in the form of turbulent
455 fluxes (Yang et al., 2017) and that the turbulent fluxes can be a major component in the energy balance during both dry and wet conditions (Steiner et al., 2018). Accounting for the debris water content through the inclusion of a simple interception storage has allowed us to identify the importance of the latent heat flux in the cooling effect of evaporation from debris during monsoon, a process that has often been neglected in previous modelling studies. We have been able to quantify how cloud overcast and additional moisture modify the energy balance of debris-covered glaciers, and especially the turbulent fluxes, to
460 result in a melt-equalizing effect.

5.1.3 Clean-ice glaciers

In contrast to debris-covered glaciers, when clean-ice glaciers are snow-free and the ice has been heated to the melting point, almost all net radiation leads directly to ice melt, while the turbulent flux contribution remains small. When entering the
465 monsoon period, the latent heat flux switches sign, changing from sublimation to condensation, which adds energy to the surface instead of removing it. This behaviour has previously been observed at sites with a 'southern influence' (Yang et al.,



2017; Azam et al., 2014), but has not been indicated for the drier conditions on the Tibetan Plateau (Mölg et al., 2012; Sun et al., 2014).

5.1.4 Dirty-ice glacier

470 At our site with thin debris, the effects that we have observed for debris-covered and clean-ice sites combine to create a melt-enhancing effect that becomes particularly potent during monsoon: the dark debris surface absorbs almost 90% of SW_{\downarrow} in the case of Hailuogou. With a short conduction length, the energy influx leads almost directly to melt. The cold surface favours condensation and a strong temperature gradient between the surface and the air (g_T pre-monsoon: -2.08 , monsoon: -2.61 $^{\circ}C m^{-1}$). Driven by higher wind speeds (Table 6, Figures A9 and A7) and moist air during monsoon, both turbulent
475 fluxes (H and LE) thus become potent sources of melt energy. This adds detail to prior observations and modelling results, that thin debris causes higher melt rates than at both clean-ice sites and sites with thicker debris cover (Reznichenko et al., 2010; Östrem, 1959; Reid and Brock, 2010; Fyffe et al., 2020), especially in humid environments (Evatt et al., 2015), e.g. the location of Hailuogou glacier.

5.2 Sensitivity of seasonal flux changes to elevation and debris thickness

480 Our results are derived from simulations at one location (AWS) on each glacier. To understand how representative they are of conditions across the glacier ablation zone at each site, and across the possible range of debris thicknesses in particular, we conduct a sensitivity experiment at each site. We re-run the model synthetically varying the AWS elevation to represent the range of elevation of each glacier ablation zone by applying a T_a lapse rate of 0.6 $^{\circ}C/100m$ and, for the debris-covered sites, by varying also the debris thickness in the range 10-80 cm (for ranges and steps see Table 7). Using the station-measured,
485 accumulated albedo is not appropriate during this experiment, due to changing snow conditions with varying elevation. We therefore include the parameterisation introduced by Ding et al. (2017) for modelling α . From the resulting range of EB flux outputs, we calculate the range of expected changes for the entire ablation zone when moving from pre-monsoon to monsoon (Δ -range). This allows us to place our results in the context of the changes that can be expected over the entire ablation zone, given its elevation span and debris thickness variability. Figure 9 shows that even accounting for the range of conditions across
490 each glacier ablation area, the pattern of pre-monsoon to monsoon difference in flux components, and importantly dQ , remain similar for debris-covered sites: The Δ -range of dQ stays within the uncertainty range, with the exception of Langtang, where the unrealistic combination of relatively thin debris and low elevation causes high dQ Δ -range. This lends confidence to the results obtained at the individual AWS locations. Although we adjusted forcing data for elevation in this exercise, we could not represent the effects of variable debris thicknesses in modifying $2m$ meteorological variables (Steiner and Pellicciotti,
495 2016; Shaw et al., 2016). This comes with the assumption that surface-atmosphere interactions are negligible compared to the altitudinal patterns and temporal changes. While this might be acceptable at thicker debris sites, it is more questionable at Hailuogou, where the observations were taken above thin and cold debris. However, also at this site, the Δ -range ends up to be small (5 $W m^{-2}$) and close to zero when debris between 10 and 80 cm thickness is applied artificially.



Table 7. Ranges of elevations and debris thicknesses used for the sensitivity runs, including the glacier terminus elevation (min), the AWS elevation (AWS) and the upper debris limit on debris-covered glaciers or to the approximated ELA elevation on clean-ice glaciers (max). We also show the range of debris thicknesses h_m modelled for debris-covered glacier sites. All combinations of elevations and debris thicknesses were used.

Glacier		Lirung	Langtang	Yala	Changri Nup	24K	Parlung No.4	Hailuogou
min	[<i>m.asl</i>]	3990	4500	5170	5270	3910	4620	2980
AWS	[<i>m.asl</i>]	4076	4557	5350	5471	3900	4800	3550
max	[<i>m.asl</i>]	4400	5600	5400	5600	4200	5400	3700
h_d [cm]		10, 20, 30, 40, 50, 60, 70, 80						

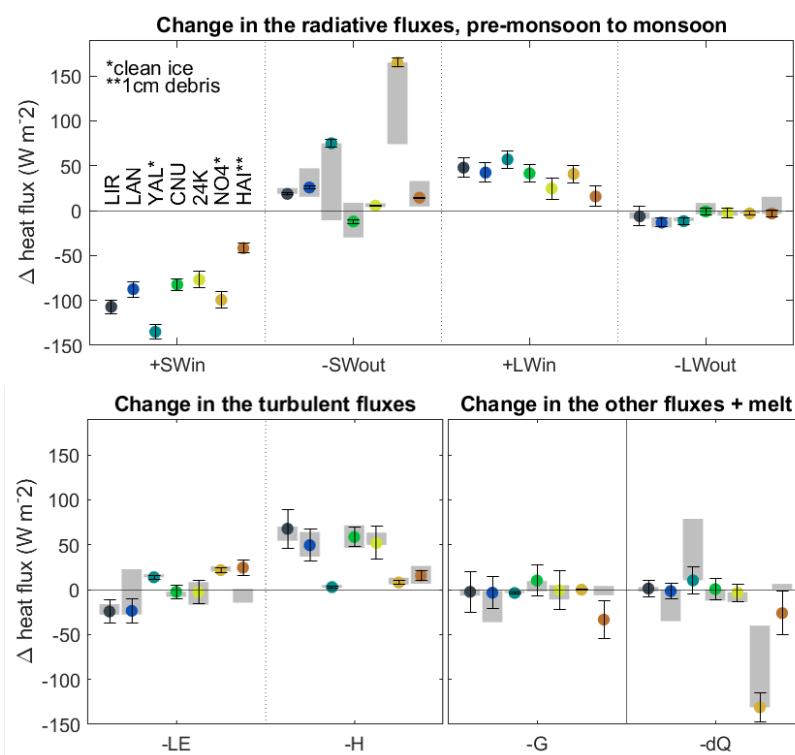


Figure 9. Changes in the individual fluxes when moving from premonsoon to monsoon. Color dots indicate 'standard' runs with AWS site specific conditions. Black bars indicate the uncertainty range on the standard runs. Grey indicates the sensitivity of flux changes (Δ -range) to debris thickness varied from 10 and 80 cm combined with the elevation range of debris-covered ablation zone of the individual glaciers;

5.3 Limitations

500 Our modelling approach allowed us to constrain the energy and mass balance at the AWS location in the best possible way for the different glacier surface types. Two debris-specific parameters (k_d and z_0) were optimised in two separate steps at the



debris sites (see section 3.3) and α was derived from measured SW_{\downarrow} and SW_{\uparrow} and given as an input at all sites. While this is not a feasible approach at the scale of entire glaciers, for application at other sites, or for future simulations, as it requires specific observations of radiation and ablation, both choices were made here in order to constrain the energy balance with observations to the greatest degree possible. Requisite data (e.g. thermistor strings, wind towers, high-resolution topography) to estimate these two parameters with established methods were not uniformly available across our study sites. These observational methods themselves can be sensitive to the measurement period (e.g. Nicholson and Benn, 2006) and are subject of ongoing research (e.g. Rounce et al., 2015; Miles et al., 2017; Rowan et al., 2020; Quincey et al., 2017), so we concluded that the calibration approach here was best suited to the application at all sites. In this respect, all optimized values fall within the expected range based on prior energy-balance studies on debris-covered glaciers (Yang et al., 2017; Rounce et al., 2015; Evatt et al., 2015; Reid and Brock, 2010; Nicholson and Benn, 2006; Rowan et al., 2020; Lejeune et al., 2013; Collier et al., 2015; McCarthy, 2018), but consistent measurements of debris parameters remain a community research priority to ensure robust modelling of sub-debris melt. To represent evaporation and the latent heat flux from the debris, we assigned an interception storage of 2 mm water to the debris surface, as, to the authors' knowledge, very few measurements have been collected of the debris layer's interception capacity and moisture content. This is important because the thermal properties of debris vary with moisture fluctuations inside the debris (Nicholson and Benn, 2006; Collier et al., 2014; Steiner et al., 2018), so the moisture retention properties of the surface debris layer may play an important role in regulating energy transfer. However, these thermal properties have been found to be stable during the core monsoon months (Rowan et al., 2020), so we kept k_d constant in time at each site in our model. Additional, targeted investigations should examine the possible role of water storage and mobility within debris layers (Giese et al., 2020; Collier et al., 2014).

5.4 Implications

Our results show that the surface type plays a large role in modulating a glaciers' response in the seasonal transition from premonsoon to monsoon: we find a melt-enhancing effect of thin debris, driven by enhanced energy uptake attributable to low albedo and turbulent energy fluxes. We also find that, on clean-ice glaciers, LE switches seasonally to become a source instead of a sink of energy to the surface, while net radiation determines melt. Importantly, we additionally identify a melt-equalizing effect of debris cover under monsoon conditions at a number of sites. Monsoon-influenced, summer-accumulation glaciers (such as Langtang, Lirung, Yala, and Changri Nup) have been previously shown to be especially vulnerable to warming due to a decrease in accumulation and an enhancement of ablation with lowering albedo (Fujita and Ageta, 2000), and our results confirm that net shortwave radiation is the key control on monsoon-period melt rates for clean ice glaciers. Our results also emphasize that the longevity of pre-monsoon snowcover into the monsoon period is a key control on melt rates, supporting past findings that the strength and timing of the monsoon onset has a profound impact on small mountain glaciers (Mölg et al., 2014, 2012) through the phase change of precipitation in the transition to monsoon conditions (Fujita and Ageta, 2000; Ding et al., 2017; Zhu et al., 2018).

The distinct responses of the surface energy balance of debris-covered and clean-ice glaciers to the pre-monsoon to monsoon transition potentially accumulate to large mass balance biases when not adequately taken into account in models. It is thus im-



portant to also consider how this seasonal transition may evolve under changing climate, and what the consequences for glacier mass balance might be. All future model simulations agree on continued warming during the 21st century over High Mountain Asia, together with a strengthening of elevation dependent warming (Palazzi et al., 2017) and increases in moisture availability. An analysis on the ensemble estimates of regionally downscaled CMIP5 projections (CORDEX) for the Himalayas (Sanjay et al., 2017) shows that total summer precipitation is projected to increase for 2036-2065 (2066-2095) by 4.4% (10.5%) in the Central Himalaya and by 6.8% (10.4%) in the Eastern Himalaya under RCP4.5 scenarios, relative to 1976-2005. While there is broad model consensus on the increase in future precipitation, there is little consensus on the future variability, frequency and spatial distribution of precipitation across High Mountain Asia (Kadel et al., 2018; Sanjay et al., 2017), which is likely a result of complex and poorly understood drivers of past monsoon changes (Saha et al., 2014; Saha and Ghosh, 2019), coarse resolution of the baseline products and topographic variability in the region (Sanjay et al., 2017). A slight shift towards an earlier monsoon onset of <5 days over the coming century together with an increasing shift towards a later retreat by 5 to 10 days (mid-century) and 10 to 15 days (end-century) might increase the length of the monsoon period, with stronger lengthening in the Eastern Himalaya (Moon and Ha, 2020).

The prospect of warmer temperatures together with increased precipitation would (1) cause a shift in the precipitation partition from snow to rain in the monsoon, resulting in snow cover shifting to higher elevations and increasing total melt; (2) potentially lead to an increase in early spring snowfall, which would delay the onset of ice melt; (3) increase the likelihood of ephemeral monsoonal snow cover but move it to higher elevations, thus leaving more of the lower ablation zones exposed; (4) increase the wetbulb temperature together with humidity to result in a reduction of the solid fraction of precipitation during monsoon. Overall it is likely that glacier ablation zones will be exposed for longer periods under future climate due to a net decrease of the snow covered duration, with a resulting increase in total ablation. A lengthening of the monsoon into autumn, on the other hand, (Moon and Ha, 2020) would somewhat offset warmer air temperatures with regards to the late-season melt for all glacier types.

Warmer and wetter monsoonal conditions, including increased cloudiness, are likely to result in an overall increase of melt rates on clean-ice and dirty-ice glaciers. This is because (1) they are more directly controlled by R_{net} , which is likely to increase in magnitude; (2) the turbulent fluxes towards cold surfaces are also likely to increase in magnitude, and they tend to 'work against' these types of glaciers. In contrast, the turbulent fluxes 'work for' debris-covered glaciers, and the melt-equalizing effect of debris under monsoon would likely remain in place. With these components summing up to have an overall protective effect on debris-covered glaciers, they are likely to resist the projected changes in the monsoonal summer longer into the future. Previous studies suggested that the mass balance of DCGs might be less sensitive to climate warming than clean-ice glaciers (e.g. Anderson and Mackintosh, 2012; Wijngaard et al., 2019; Mattson, 2000). Here we confirm this hypothesis and suggest that this is even more the case under monsoonal conditions.

Simplified methods of glacier melt calculation (e.g. relying only on temperature or temperature and shortwave radiation) may integrate some of these processes through calibration (e.g. Ragettli et al., 2016). However, in a study on two clean-ice glaciers (Yala and Mera), Litt et al. (2019) were able to transfer Temperature Index and Enhanced Temperature Index models between sites and years only during pre-monsoon. During monsoon, the transfer failed due to site-specific and inter-annually variable



cloudiness.

5.5 Future work

By modelling seven different study glaciers across the Himalayan arc, we have been able to identify important monsoon effects on the energy and mass balance of debris-covered and clean-ice glaciers. In the context of the large spatial and inter-annual variability in the climate, including the monsoon strength and timing, our sample size remains small due to data availability. The timing and quantity of spring snow-cover and monsoonal snowfalls have large effects on the energy and mass balance, and these variables can be highly variable between years. A future analysis could leverage a greater number of complete AWS records, and possibly multi-year records, in order to extend some of our findings. Despite the advanced representation in Tethys-Chloris, the surfaces of glaciers, and especially of debris-covered glaciers, are more complex systems than indicated at the AWS location. Future work should be invested into spatially distributing forcing data and parameters necessary to run energy-balance models in a distributed framework at glacier and catchment scales. Studies employing distributed energy balance models could, for example, test the melt-equalizing effect of debris at the glacier scale and its overall effect on the catchment runoff. This could be combined with generating spatially consistent forcing data using high-resolution weather modelling as in Bonekamp et al. (2019) or Potter et al. (2020), and expanded to larger domains. Realistic representations of the glacier surface, including distributed debris thickness, and supraglacial features, such as ice cliffs and surface ponds, should also be established to provide well-constrained water budgets and improved representations of glacierised environments in land-surface models under present and future environmental conditions.

6 Conclusions

By modelling the energy and mass balance of seven glaciers in the Himalayas at on-glacier weather stations, we identify and explain the main effects on the energy and mass balance caused by the Indian and East Asian summer monsoons. Heavy cloud cover, liquid precipitation, wind speed, the presence and thickness of debris cover, and elevation shape the energy and mass balances of the Himalayan glaciers during the ablation season. The timing of snow melt-out and the presence of ephemeral monsoonal snowcover play a particularly important role, especially at high elevations. We highlight key pre-monsoon to monsoon changes in energy fluxes, distinct for clean-ice and debris-covered glacier sites: the melt of clean-ice glaciers is primarily radiation-driven at any point during the ablation season, and strongly influenced by albedo variations. The latent heat flux can initially be a small sink and turn into a source during the core monsoon. Debris cover can act in two ways: (1) Once a debris layer of a few centimetres is established, it returns most of the heat it absorbs back to the atmosphere via longwave and turbulent heat fluxes. The sensible heat flux reduces during core monsoon, but the latent heat flux removes energy from the surface due to evaporation of liquid water. The turbulent fluxes readjust in this way to monsoonal temperature, wind and moisture regimes, maintaining a nearly constant melt rate over the entire ablation period. Sensitivity analyses of our energy-balance model shows that these findings hold for large portions of the debris-covered glacier surfaces. (2) When it is thin, debris amplifies the in-



605 coming energy due to its dark and cold surface, small conduction distance to the ice and sensitivity to turbulence. The turbulent fluxes 'work for' the debris-covered glaciers by returning absorbed energy to the atmosphere, and tend to 'work against' clean-ice and dirty-ice glaciers under monsoonal conditions. We thus expect the mass balance of debris-covered glaciers to react less sensitively to projected future monsoon changes than clean-ice and dirty-ice glaciers.



Code and data availability. Model and analysis codes as well as AWS datasets are available upon request during the discussion and review phase and will be made publicly available at a later stage.

610 *Author contributions.* SFu, FP and EM designed the study. SFu carried out the analysis with the help of CF, MM and SFa. SFu interpreted the results, created the figures and wrote the manuscript with the help of CF, EM, MM, TS and FP. SFa, PW, WI, and QL reviewed the manuscript. WY and BD facilitated field data collection and provided parameterisations for albedo and precipitation phase. WY, PW and WI also contributed data sets.

Competing interests. The authors declare that they have no conflict of interest.

615 *Acknowledgements.* This project has received funding from the European Research Council (ERC) under the European Union's Horizon 2020 research and innovation programme (grant agreement No 772751), RAVEN, "Rapid mass losses of debris covered glaciers in High Mountain Asia". We would like to thank Jakob Steiner and ICIMOD for hosting and contributing data sets. We also thank Marin Kneib for organizing and helping with field data collection and Achille Jouberton for commenting on the manuscript.



Appendix A

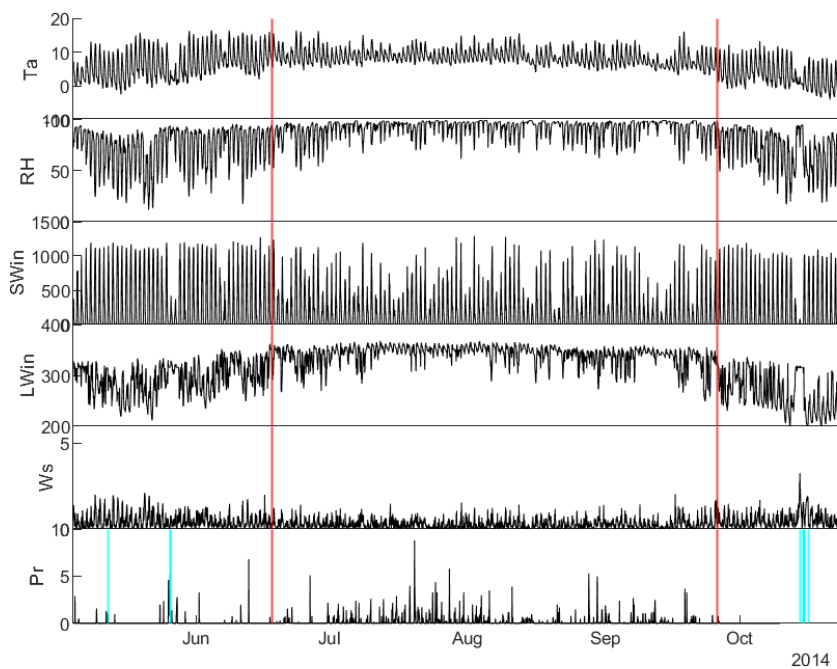


Figure A1. Meteorological observations on Lirung during the ablation season recorded by AWS; Red vertical lines indicate monsoon onset and end; Blue indicates time steps with snow cover at the AWS location, as determined from α (>0.5)

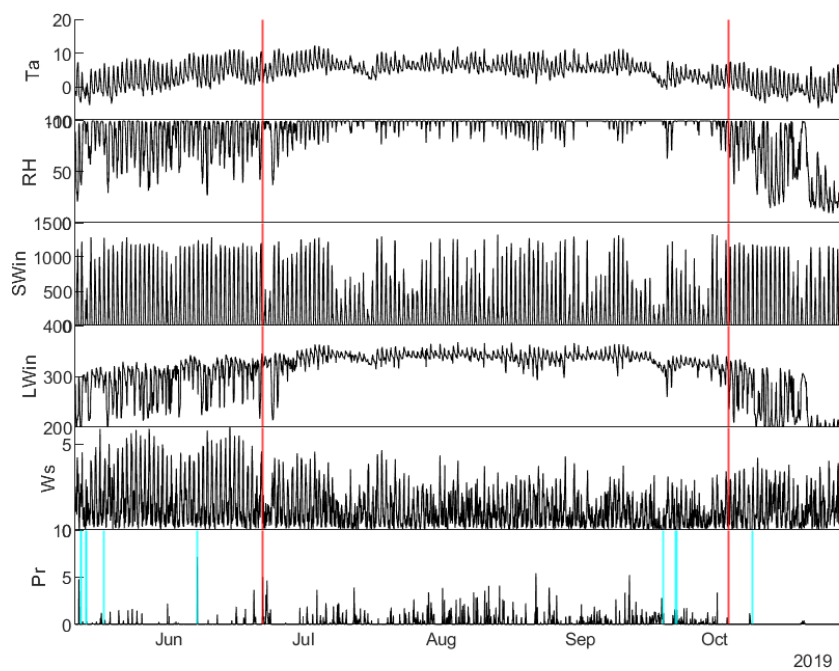


Figure A2. Meteorological observations on Langtang during the ablation season recorded by AWS; Red vertical lines indicate monsoon onset and end; Blue indicates time steps with snow cover at the AWS location, as determined from α (>0.5)

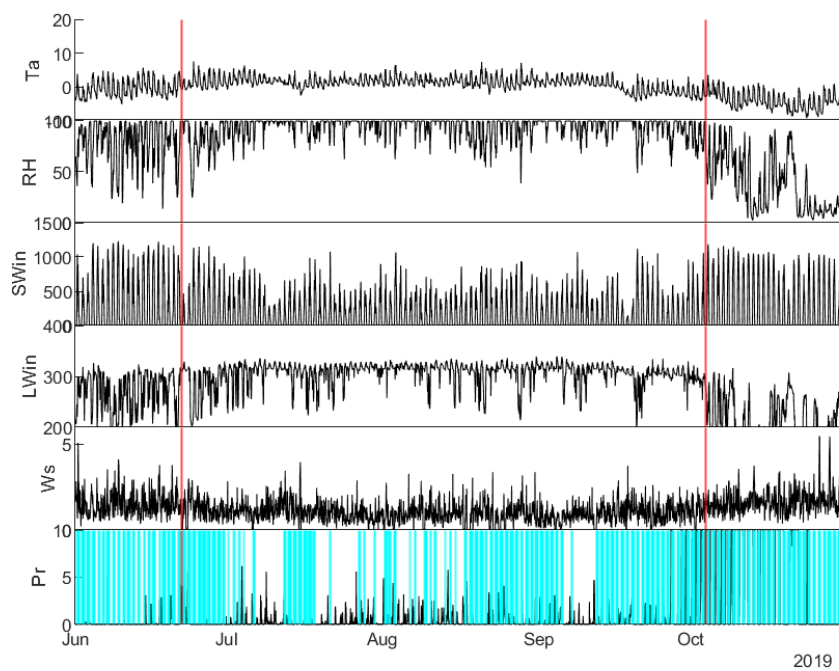


Figure A3. Meteorological observations on Yala during the ablation season recorded by AWS; Red vertical lines indicate monsoon onset and end; Blue indicates time steps with snow cover at the AWS location, as determined from α (>0.5)

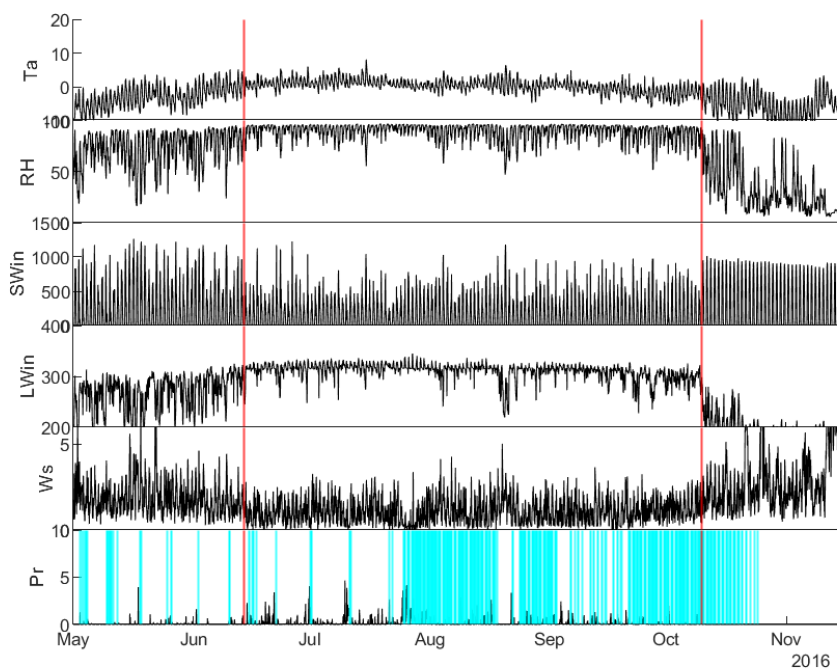


Figure A4. Meteorological observations on Changri Nup during the ablation season recorded by AWS; Red vertical lines indicate monsoon onset and end; Blue indicates time steps with snow cover at the AWS location, as determined from α (>0.5)

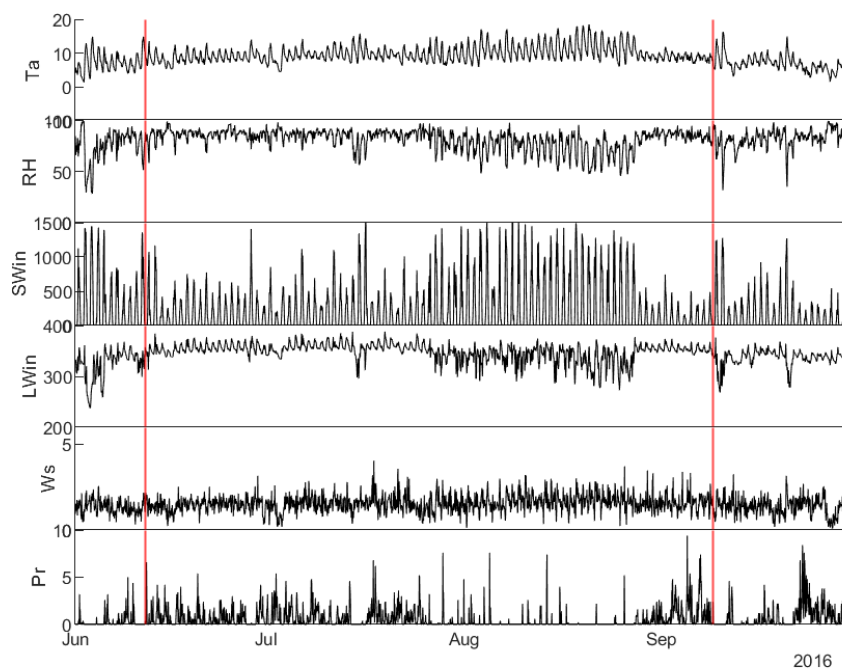


Figure A5. Meteorological observations on 24K during the ablation season recorded by AWS; Red vertical lines indicate monsoon onset and end; Blue indicates time steps with snow cover at the AWS location, as determined from α (>0.5)

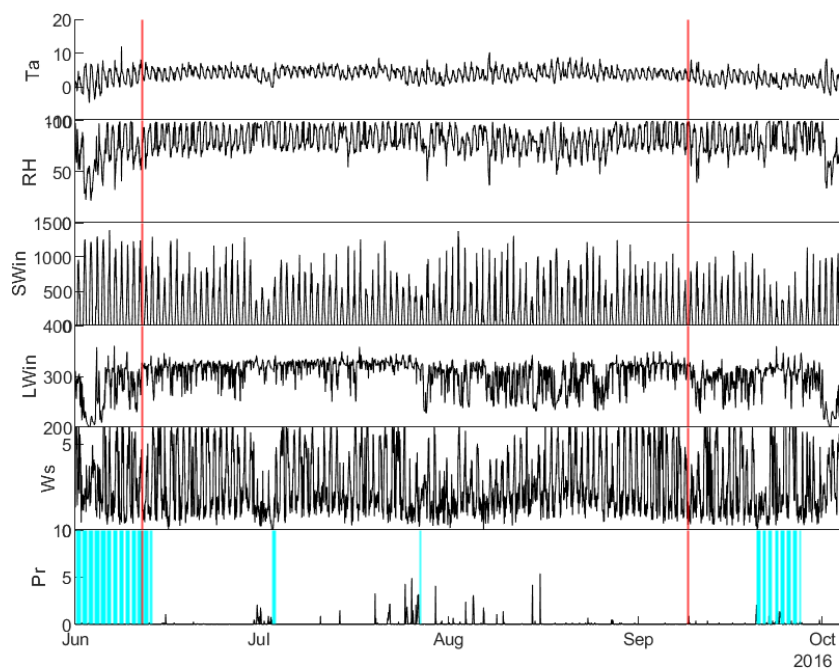


Figure A6. Meteorological observations on Parlung No.4 during the ablation season recorded by AWS; Red vertical lines indicate monsoon onset and end; Blue indicates time steps with snow cover at the AWS location, as determined from α (>0.5)

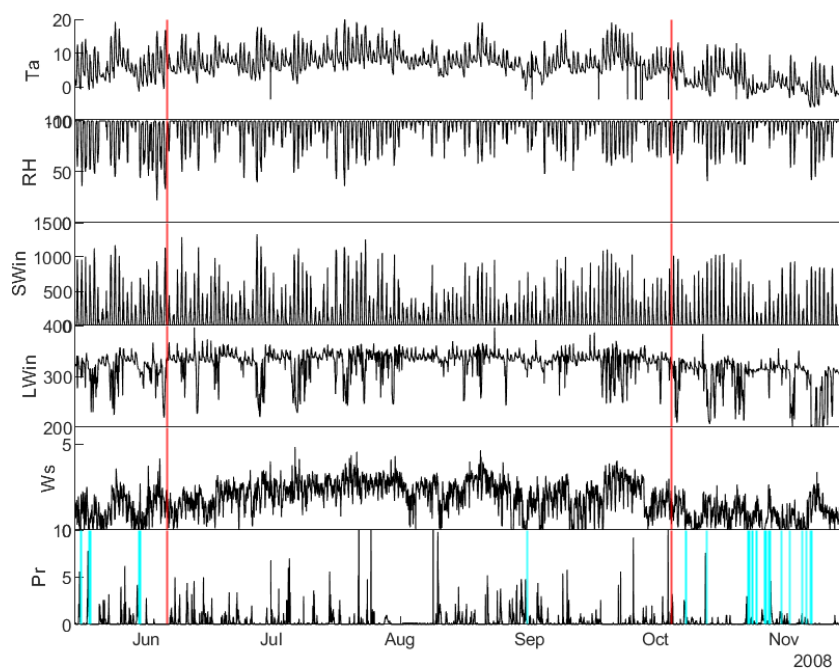


Figure A7. Meteorological observations on Hailuogou during the ablation season recorded by AWS; Red vertical lines indicate monsoon onset and end; Blue indicates time steps with snow cover at the AWS location, as determined from α (>0.5)

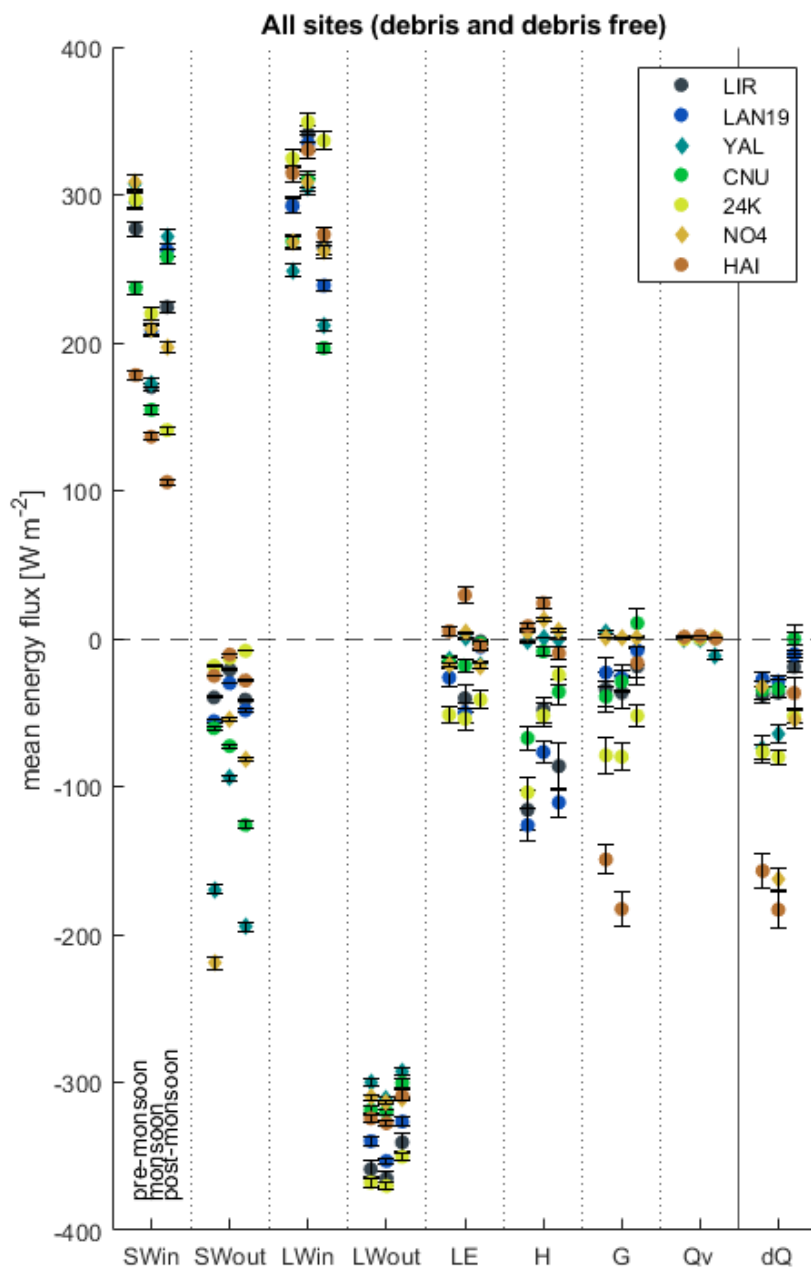


Figure A8. All energy balance components of all glaciers in comparison, split into pre-monsoon, monsoon, post-monsoon; black bars indicate the uncertainty range;

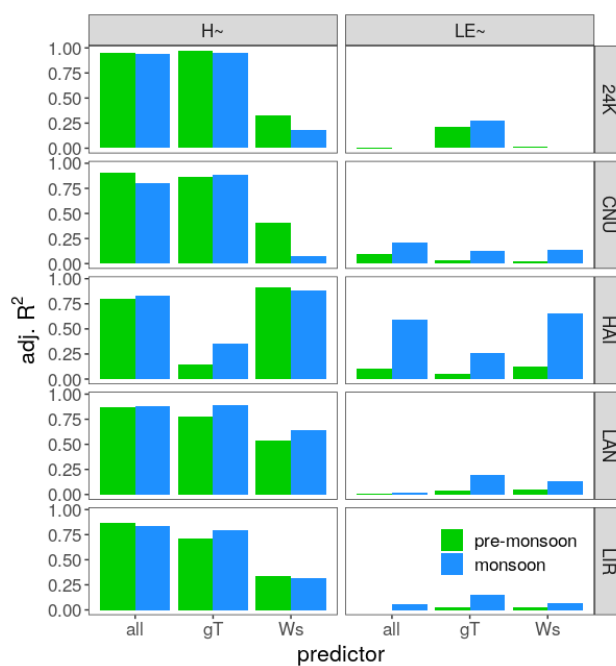


Figure A9. Predictive power of temperature gradient between surface and air (gT) and wind speed (Ws) and their combination for determining H and LE . 'All' indicates a multiple polynomial regression model using both variables, otherwise a univariate polynomial regression model was used, and both models had 2 degrees of freedom.

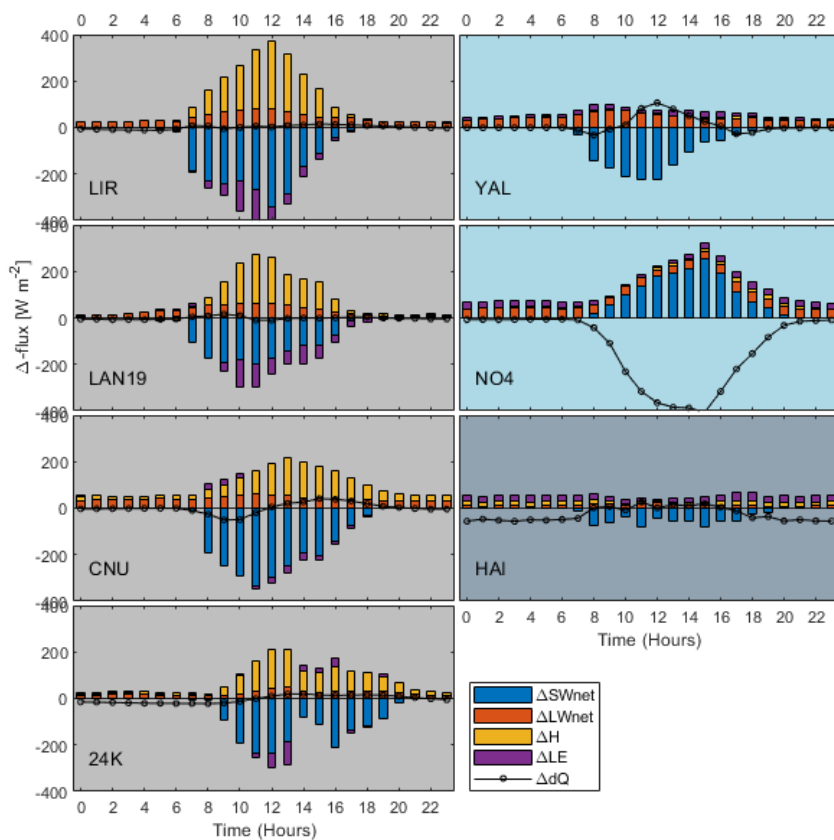


Figure A10. Energy flux differences in the diurnal cycle (stacked) between pre-monsoon and monsoon; The direction of change is to be considered relative to the sign of the original flux. Fluxes towards/away from the surface have a positive/negative sign. For example, a positive change in a negative flux means a reduction in the magnitude flux, and can also lead to a change in sign. Grey background indicates debris covered site; light blue indicates clean ice sites; grey-blue indicates 1cm debris site



620 References

- Anderson, B. and Mackintosh, A.: Controls on mass balance sensitivity of maritime glaciers in the Southern Alps, New Zealand: the role of debris cover, *Journal of Geophysical Research: Earth Surface*, 117, 2012.
- Azam, M., Wagnon, P., Vincent, C., Ramanathan, A., Favier, V., Mandal, A., and Pottakkal, J.: Processes governing the mass balance of Chhota Shigri Glacier (western Himalaya, India) assessed by point-scale surface energy balance measurements, *Cryosphere*, 8, 2195–2217, 2014.
- 625 B elair, S., Crevier, L.-P., Mailhot, J., Bilodeau, B., and Delage, Y.: Operational implementation of the ISBA land surface scheme in the Canadian regional weather forecast model. Part I: Warm season results, *Journal of hydrometeorology*, 4, 352–370, 2003.
- Bonekamp, P. N., de Kok, R. J., Collier, E., and Immerzeel, W. W.: Contrasting meteorological drivers of the glacier mass balance between the Karakoram and central Himalaya, *Frontiers in Earth Science*, 7, 107, 2019.
- 630 Bookhagen, B. and Burbank, D. W.: Toward a complete Himalayan hydrological budget: Spatiotemporal distribution of snowmelt and rainfall and their impact on river discharge, *Journal of Geophysical Research: Earth Surface*, 115, 2010.
- Botter, M., Zeeman, M., Burlando, P., and Fatichi, S.: Impacts of fertilization on grassland productivity and water quality across the European Alps: insights from a mechanistic model, *Biogeosciences Discussions*, pp. 1–35, 2020.
- Brock, B. W., Willis, I. C., and Sharp, M. J.: Measurement and parameterization of albedo variations at Haut Glacier d’Arolla, Switzerland, 635 *Journal of Glaciology*, 46, 675–688, 2000.
- Brun, F., Berthier, E., Wagnon, P., K aab, A., and Treichler, D.: A spatially resolved estimate of High Mountain Asia glacier mass balances from 2000 to 2016, *Nature geoscience*, 10, 668–673, 2017.
- Collier, E. and Immerzeel, W. W.: High-resolution modeling of atmospheric dynamics in the Nepalese Himalaya, *Journal of Geophysical Research: Atmospheres*, 120, 9882–9896, 2015.
- 640 Collier, E., Nicholson, L., Brock, B., Maussion, F., Essery, R., and Bush, A.: Representing moisture fluxes and phase changes in glacier debris cover using a reservoir approach, *The Cryosphere*, 8, 1429–1444, 2014.
- Collier, E., Maussion, F., Nicholson, L., M olgl, T., Immerzeel, W., and Bush, A.: Impact of debris cover on glacier ablation and atmosphere-glacier feedbacks in the Karakoram, 2015.
- Cuffey, K. M. and Paterson, W. S. B.: *The physics of glaciers*, Academic Press, 2010.
- 645 Ding, B., Yang, K., Qin, J., Wang, L., Chen, Y., and He, X.: The dependence of precipitation types on surface elevation and meteorological conditions and its parameterization, *Journal of hydrology*, 513, 154–163, 2014.
- Ding, B., Yang, K., Yang, W., He, X., Chen, Y., Guo, X., Wang, L., Wu, H., and Yao, T.: Development of a Water and Enthalpy Budget-based Glacier mass balance Model (WEB-GM) and its preliminary validation, *Water Resources Research*, 53, 3146–3178, 2017.
- Evatt, G. W., Abrahams, I. D., Heil, M., Mayer, C., Kingslake, J., Mitchell, S. L., Fowler, A. C., and Clark, C. D.: Glacial melt under a porous 650 debris layer, *Journal of Glaciology*, 61, 825–836, 2015.
- Farinotti, D., Huss, M., F urst, J. J., Landmann, J., Machguth, H., Maussion, F., and Pandit, A.: A consensus estimate for the ice thickness distribution of all glaciers on Earth, *Nature Geoscience*, 12, 168–173, 2019.
- Farinotti, D., Immerzeel, W. W., de Kok, R. J., Quincey, D. J., and Dehecq, A.: Manifestations and mechanisms of the Karakoram glacier Anomaly, *Nature Geoscience*, 13, 8–16, 2020.



- 655 Fatichi, S., Ivanov, V. Y., and Caporali, E.: A mechanistic ecohydrological model to investigate complex interactions in cold and warm water-controlled environments: 1. Theoretical framework and plot-scale analysis, *Journal of Advances in Modeling Earth Systems*, 4, 2012.
- Fujita, K Sakai, A. et al.: Modelling runoff from a Himalayan debris-covered glacier, *Hydrol. Earth Syst. Sci*, 18, 2679–2694, 2014.
- Fujita, K. and Ageta, Y.: Effect of summer accumulation on glacier mass balance on the Tibetan Plateau revealed by mass-balance model, 660 *Journal of Glaciology*, 46, 244–252, 2000.
- Fujita, K., Takeuchi, N., and Seko, K.: Glaciological observations of Yala Glacier in Langtang Valley, Nepal Himalayas, 1994 and, *Bulletin of Glacier Research*, 16, 75–8, 1998.
- Fyffe, C. L., Woodget, A. S., Kirkbride, M. P., Deline, P., Westoby, M. J., and Brock, B. W.: Processes at the margins of supraglacial debris cover: quantifying dirty ice ablation and debris redistribution, *Earth Surface Processes and Landforms*, 2020.
- 665 Gardelle, J., Berthier, E., and Arnaud, Y.: Slight mass gain of Karakoram glaciers in the early twenty-first century, *Nature geoscience*, 5, 322–325, 2012.
- Giese, A., Boone, A., Wagnon, P., and Hawley, R.: Incorporating moisture content in surface energy balance modeling of a debris-covered glacier, *The Cryosphere*, 14, 1555–1577, 2020.
- Herreid, S. and Pellicciotti, F.: The state of rock debris covering Earth’s glaciers, *Nature Geoscience*, pp. 1–7, 2020.
- 670 Heynen, M., Miles, E., Ragettli, S., Buri, P., Immerzeel, W. W., and Pellicciotti, F.: Air temperature variability in a high-elevation Himalayan catchment, *Annals of Glaciology*, 57, 212–222, 2016.
- ICIMOD: AWS Yala Glacier [Data set]. ICIMOD., 2021.
- Immerzeel, W. W., Van Beek, L., Konz, M., Shrestha, A., and Bierkens, M.: Hydrological response to climate change in a glacierized catchment in the Himalayas, *Climatic change*, 110, 721–736, 2012.
- 675 Immerzeel, W. W., Kraaijenbrink, P. D., Shea, J., Shrestha, A. B., Pellicciotti, F., Bierkens, M. F., and de Jong, S. M.: High-resolution monitoring of Himalayan glacier dynamics using unmanned aerial vehicles, *Remote Sensing of Environment*, 150, 93–103, 2014.
- Kadel, I., Yamazaki, T., Iwasaki, T., and Abdillahi, M. R.: Projection of future monsoon precipitation over the central Himalayas by CMIP5 models under warming scenarios, *Climate Research*, 75, 1–21, 2018.
- Kaser, G., Großhauser, M., and Marzeion, B.: Contribution potential of glaciers to water availability in different climate regimes, *Proceedings of the National Academy of Sciences*, 107, 20 223–20 227, 2010.
- 680 Kraaijenbrink, P., Bierkens, M., Lutz, A., and Immerzeel, W.: Impact of a global temperature rise of 1.5 degrees Celsius on Asia’s glaciers, *Nature*, 549, 257–260, 2017.
- Kumar, K. K., Rajagopalan, B., Hoerling, M., Bates, G., and Cane, M.: Unraveling the mystery of Indian monsoon failure during El Niño, *Science*, 314, 115–119, 2006.
- 685 Lejeune, Y., Bertrand, J.-M., Wagnon, P., and Morin, S.: A physically based model of the year-round surface energy and mass balance of debris-covered glaciers, *Journal of Glaciology*, 59, 327–344, 2013.
- Liao, H., Liu, Q., Zhong, Y., and Lu, X.: Landsat-based estimation of the glacier surface temperature of Hailuoguo glacier, Southeastern Tibetan Plateau, between 1990 and 2018, *Remote Sensing*, 12, 2105, 2020.
- Litt, M., Shea, J., Wagnon, P., Steiner, J., Koch, I., Stigter, E., and Immerzeel, W.: Glacier ablation and temperature indexed melt models in 690 the Nepalese Himalaya, *Scientific reports*, 9, 1–13, 2019.
- Mascart, P., Noilhan, J., and Giordani, H.: A modified parameterization of flux-profile relationships in the surface layer using different roughness length values for heat and momentum, *Boundary-Layer Meteorology*, 72, 331–344, 1995.



- Mastrotheodoros, T., Pappas, C., Molnar, P., Burlando, P., Manoli, G., Parajka, J., Rigon, R., Szeles, B., Bottazzi, M., Hadjidoukas, P., et al.: More green and less blue water in the Alps during warmer summers, *Nature Climate Change*, 10, 155–161, 2020.
- 695 Mattson, L. E.: The influence of a debris cover on the mid-summer discharge of Dome Glacier, Canadian Rocky Mountains, *IAHS PUBLICATION*, pp. 25–34, 2000.
- Maussion, F., Scherer, D., Mölg, T., Collier, E., Curio, J., and Finkelnburg, R.: Precipitation seasonality and variability over the Tibetan Plateau as resolved by the High Asia Reanalysis, *Journal of Climate*, 27, 1910–1927, 2014.
- McCarthy, M. J.: Quantifying supraglacial debris thickness at local to regional scales, Ph.D. thesis, Scott Polar Research Institute and British Antarctic Survey, 2018.
- 700 Miles, E. S., Steiner, J. F., and Brun, F.: Highly variable aerodynamic roughness length (z_0) for a hummocky debris-covered glacier, *Journal of Geophysical Research: Atmospheres*, 122, 8447–8466, 2017.
- Mölg, T., Maussion, F., Yang, W., and Scherer, D.: The footprint of Asian monsoon dynamics in the mass and energy balance of a Tibetan glacier, *The Cryosphere*, 6, 1445, 2012.
- 705 Mölg, T., Maussion, F., and Scherer, D.: Mid-latitude westerlies as a driver of glacier variability in monsoonal High Asia, *Nature Climate Change*, 4, 68–73, 2014.
- Moon, S. and Ha, K.-J.: Future changes in monsoon duration and precipitation using CMIP6, *npj Climate and Atmospheric Science*, 3, 1–7, 2020.
- Muñoz Sabater, J.: ERA5-Land monthly averaged data from 1981 to present .Copernicus Climate Change Service (C3S) Climate Data Store (CDS). (Accessed on 01-10-2020), 2019.
- 710 Nicholson, L. and Benn, D. I.: Calculating ice melt beneath a debris layer using meteorological data, *Journal of Glaciology*, 52, 463–470, 2006.
- Nicholson, L. and Stiperski, I.: Comparison of turbulent structures and energy fluxes over exposed and debris-covered glacier ice, *Journal of Glaciology*, 66, 543–555, 2020.
- 715 Noilhan, J. and Mahfouf, J.-F.: The ISBA land surface parameterisation scheme, *Global and planetary Change*, 13, 145–159, 1996.
- Östrem, G.: Ice melting under a thin layer of moraine, and the existence of ice cores in moraine ridges, *Geografiska Annaler*, 41, 228–230, 1959.
- Palazzi, E., Filippi, L., and von Hardenberg, J.: Insights into elevation-dependent warming in the Tibetan Plateau-Himalayas from CMIP5 model simulations, *Climate Dynamics*, 48, 3991–4008, 2017.
- 720 Paschalis, A., Fatichi, S., Pappas, C., and Or, D.: Covariation of vegetation and climate constrains present and future T/ET variability, *Environmental Research Letters*, 13, 104012, 2018.
- Potter, E. R., Orr, A., Willis, I. C., Bannister, D., and Wagnon, P.: Meteorological impacts of a novel debris-covered glacier category in a regional climate model across a Himalayan catchment, *Atmospheric Science Letters*, p. e1018, 2020.
- Quincey, D., Smith, M., Rounce, D., Ross, A., King, O., and Watson, C.: Evaluating morphological estimates of the aerodynamic roughness of debris covered glacier ice, *Earth Surface Processes and Landforms*, 42, 2541–2553, 2017.
- 725 Ragettli, S., Pellicciotti, F., Immerzeel, W. W., Miles, E. S., Petersen, L., Heynen, M., Shea, J. M., Stumm, D., Joshi, S., and Shrestha, A.: Unraveling the hydrology of a Himalayan catchment through integration of high resolution in situ data and remote sensing with an advanced simulation model, *Advances in Water Resources*, 78, 94–111, 2015.
- Ragettli, S., Immerzeel, W. W., and Pellicciotti, F.: Contrasting climate change impact on river flows from high-altitude catchments in the Himalayan and Andes Mountains, *Proceedings of the National Academy of Sciences*, 113, 9222–9227, 2016.
- 730



- Reid, T. D. and Brock, B. W.: An energy-balance model for debris-covered glaciers including heat conduction through the debris layer, *Journal of Glaciology*, 56, 903–916, 2010.
- Reznichenko, N., Davies, T., Shulmeister, J., and McSaveney, M.: Effects of debris on ice-surface melting rates: an experimental study, *Journal of Glaciology*, 56, 384–394, 2010.
- 735 Rounce, D., Quincey, D., and McKinney, D.: Debris-covered glacier energy balance model for Imja-Lhotse Shar Glacier in the Everest region of Nepal, 2015.
- Rowan, A. V., Nicholson, L. I., Quincey, D. J., Gibson, M. J., Irvine-Fynn, T. D., Watson, C. S., Wagnon, P., Rounce, D. R., Thompson, S. S., Porter, P. R., et al.: Seasonally stable temperature gradients through supraglacial debris in the Everest region of Nepal, Central Himalaya, *Journal of Glaciology*, pp. 1–12, 2020.
- 740 Saha, A. and Ghosh, S.: Can the weakening of Indian Monsoon be attributed to anthropogenic aerosols?, *Environmental Research Communications*, 1, 061 006, 2019.
- Saha, A., Ghosh, S., Sahana, A., and Rao, E.: Failure of CMIP5 climate models in simulating post-1950 decreasing trend of Indian monsoon, *Geophysical Research Letters*, 41, 7323–7330, 2014.
- Sakai, A. and Fujita, K.: Contrasting glacier responses to recent climate change in high-mountain Asia, *Scientific reports*, 7, 1–8, 2017.
- 745 Sakai, A., Fujita, K., and Kubota, J.: Evaporation and percolation effect on melting at debris-covered Lirung Glacier, Nepal Himalayas, 1996, *Bulletin of glaciological research*, 21, 9–16, 2004.
- Sanjay, J., Krishnan, R., Shrestha, A. B., Rajbhandari, R., and Ren, G.-Y.: Downscaled climate change projections for the Hindu Kush Himalayan region using CORDEX South Asia regional climate models, *Advances in Climate Change Research*, 8, 185–198, 2017.
- Scherler, D., Bookhagen, B., and Strecker, M. R.: Hillslope-glacier coupling: The interplay of topography and glacial dynamics in High Asia, *Journal of Geophysical Research: Earth Surface*, 116, 2011a.
- 750 Scherler, D., Bookhagen, B., and Strecker, M. R.: Spatially variable response of Himalayan glaciers to climate change affected by debris cover, *Nature geoscience*, 4, 156–159, 2011b.
- Shah, S. S., Banerjee, A., Nainwal, H. C., and Shankar, R.: Estimation of the total sub-debris ablation from point-scale ablation data on a debris-covered glacier, *Journal of Glaciology*, 65, 759–769, 2019.
- 755 Shaw, T. E., Brock, B. W., Fyffe, C. L., Pellicciotti, F., Rutter, N., and Diotri, F.: Air temperature distribution and energy-balance modelling of a debris-covered glacier, *Journal of Glaciology*, 62, 185–198, 2016.
- Shean, D., Bhushan, S., Montesano, P., Rounce, D., Arendt, A., and Osmanoglu, B.: A systematic, regional assessment of High Mountain Asia Glacier mass balance. *Front, Earth Sci*, 7, 363, 2020.
- Shrestha, R., Kayastha, R., and Kayastha, R.: Effect of debris on seasonal ice melt (2016- 2018) on Ponkar Glacier, Manang, Nepal. *Sciences in Cold and Arid Regions*, 12 (5): 261- 271. DOI: 10.3724/SP. J. 1226.2020. 00261, Reejju Shrestha et al, pp. 0261–0271, 2020.
- 760 Steiner, J. F. and Pellicciotti, F.: Variability of air temperature over a debris-covered glacier in the Nepalese Himalaya, *Annals of Glaciology*, 57, 295–307, 2016.
- Steiner, J. F., Litt, M., Stigter, E. E., Shea, J., Bierkens, M. F., and Immerzeel, W. W.: The importance of turbulent fluxes in the surface energy balance of a debris-covered glacier in the Himalayas, *Frontiers in Earth Science*, 6, 144, 2018.
- 765 Stumm, D., Joshi, S. P., Gurung, T. R., and Silwal, G.: Mass balances of Yala and Rikha Samba Glacier, Nepal from 2000 to 2017, *Earth System Science Data Discussions*, pp. 1–37, 2020.
- Sun, W., Qin, X., Du, W., Liu, W., Liu, Y., Zhang, T., Xu, Y., Zhao, Q., Wu, J., and Ren, J.: Ablation modeling and surface energy budget in the ablation zone of Laohugou glacier No. 12, western Qilian mountains, China, *Annals of glaciology*, 55, 111–120, 2014.



- van den Broeke, M., van As, D., Reijmer, C., and van de Wal, R.: Assessing and improving the quality of unattended radiation observations
770 in Antarctica, *Journal of Atmospheric and Oceanic Technology*, 21, 1417–1431, 2004.
- Verseghy, D. L.: CLASS—A Canadian land surface scheme for GCMs. I. Soil model, *International Journal of Climatology*, 11, 111–133,
1991.
- Vincent, C., Wagnon, P., Shea, J., Immerzeel, W., Kraaijenbrink, P., Shrestha, D., Soruco, A., Arnaud, Y., Brun, F., Berthier, E., et al.:
Reduced melt on debris-covered glaciers: investigations from Changri Nup Glacier, Nepal, 2016.
- 775 Wagnon, P.: IACS working group on debris-covered glaciers. AWS North Changri Nup Glacier [Data set]. Hosted on glacioclim.osug.fr,
2021.
- Wijngaard, R. R., Steiner, J. F., Kraaijenbrink, P. D., Klug, C., Adhikari, S., Banerjee, A., Pellicciotti, F., Van Beek, L. P., Bierkens, M. F.,
Lutz, A. F., et al.: Modeling the Response of the Langtang Glacier and the Hintereisferner to a Changing Climate Since the Little Ice Age,
Frontiers in Earth Science, 7, 143, 2019.
- 780 Yang, W., Guo, X., Yao, T., Yang, K., Zhao, L., Li, S., and Zhu, M.: Summertime surface energy budget and ablation modeling in the ablation
zone of a maritime Tibetan glacier, *Journal of Geophysical Research: Atmospheres*, 116, 2011.
- Yang, W., Yao, T., Zhu, M., and Wang, Y.: Comparison of the meteorology and surface energy fluxes of debris-free and debris-covered
glaciers in the southeastern Tibetan Plateau, *Journal of Glaciology*, 63, 1090–1104, 2017.
- Yao, T., Thompson, L., Yang, W., Yu, W., Gao, Y., Guo, X., Yang, X., Duan, K., Zhao, H., Xu, B., et al.: Different glacier status with
785 atmospheric circulations in Tibetan Plateau and surroundings, *Nature climate change*, 2, 663–667, 2012.
- Zhang, Y., Fujita, K., Liu, S., Liu, Q., and Nuimura, T.: Distribution of debris thickness and its effect on ice melt at Hailuoguo glacier,
southeastern Tibetan Plateau, using in situ surveys and ASTER imagery, *Journal of Glaciology*, 57, 1147–1157, 2011.
- Zhu, M., Yao, T., Yang, W., Xu, B., Wu, G., and Wang, X.: Differences in mass balance behavior for three glaciers from different climatic
regions on the Tibetan Plateau, *Climate Dynamics*, 50, 3457–3484, 2018.